An exploration of the production of negative ions from neutral gases using a negative hydrogen ion source driver

by

Andrew Paul

B.Eng., Carleton University, 2019

A Thesis Submitted in Partial Fulfillment of the Requirements for the Degree of

MASTER OF SCIENCE

in the Department of Physics and Astronomy

©Andrew Paul, 2023
University of Victoria

All rights reserved. This thesis may not be reproduced in whole or in part, by photocopy or other means, without the permission of the author.

We acknowledge and respect the lək^{w}ənən peoples on whose traditional territory the university stands and the Songhees, Esquimalt and W̱SÁNEĆ peoples whose historical relationships with the land continue to this day. We would also like to acknowledge that the research carried out for this project was done so on the traditional territory of the Sinixt, the Ktunaxa, and the Syilx peoples who we will continue to learn from.

An exploration of the production of negative ions from neutral gases using a negative hydrogen ion source driver

by

Andrew Paul

B.Eng., Carleton University, 2019

Supervisory Committee

Dr. Tobias Junginger, Supervisor
Department of Physics and Astronomy

Dr. Morgan Dehnel, Industrial Supervisor
D-Pace Inc.
Adjunct Professor, University of Victoria

Abstract

Negative ion beams have wide-ranging applications from acceleration in cyclotrons for medical radioisotope production to areas where tandem accelerators are leveraged. The fields in which tandem accelerators are used include nuclear structure research, environmental studies, materials characterization, medical treatments and ion implantation in semiconductor devices. A commercially important case where negative helium ions are utilized is in the semiconductor industry where they are conventionally created by double-charge exchange ion sources using metallic vapours (typically Alkali's). These metallic vapours lead to challenges such as contamination, electrical shorts, and maintenance difficulties. In an effort to overcome the significant disadvantage of metallic vapour charge exchange, this thesis will firstly investigate the production of negative helium ions using a non-metallic charge exchange method in which negative hydrogen ions will be impinged upon neutral helium gas. A charge exchange cell is developed for this project which includes an electrostatic accelerator to accelerate newly produced negative ions from the target gas. The main objective focuses on negative helium ion production but the method is applied to different gas targets including H_2, CO_2, and O_2 with the goal of accelerating and measuring negative ions that are the products of these targets. This approach aims to avoid the significant contamination issues from the metallic vapour double-charge exchange method and explore novel methods for negative ion production via charge transfer.

Contents

List of Tables

List of Figures

Acknowledgements

I would firstly like to acknowledge and give an incredible amount of thanks to my industrial research supervisor Dr. Morgan Dehnel for giving me this opportunity and for the guidance and much needed moral support along the way. I would also like to thank Dr. Tobias Junginger, my academic supervisor, for taking me on as a student and teaching me a great deal of accelerator physics.
I can't thank Dr. Stéphane Melanson enough for the constant technical and intellectual support, I could not have accomplished this amount of work without his guidance. I would like to thank Dr. Anand George for teaching me how to operate the ISTF and taking the time to explain the fundamental operation of the H^- ion source. I would like to extend a huge amount of gratitude to all of the staff at D-Pace for their kindness and willingness to answer any of my questions.
I would like to acknowledge Dr. Søren Pape Møller for the co-creation of the original concept for this method of negative ion production which is explored. Finally, I would like to thank Mitacs national research organization for the financial support which has been paramount to this research.

Chapter 1

Introduction

Ion beams are widely used in a multitude of industries from material science to environmental sciences, nuclear structure analysis and many medical applications [1]. In particular, negative ion beams are found to be useful when higher energy direct current (DC) beams are required. These high energy beams can be created using a tandem accelerator which strips two electrons from an incident negative ion beam with a positive potential electrode in order to double the energy of the ion beam [2]. A diagram of a simplified tandem accelerator is shown in figure 1.1.

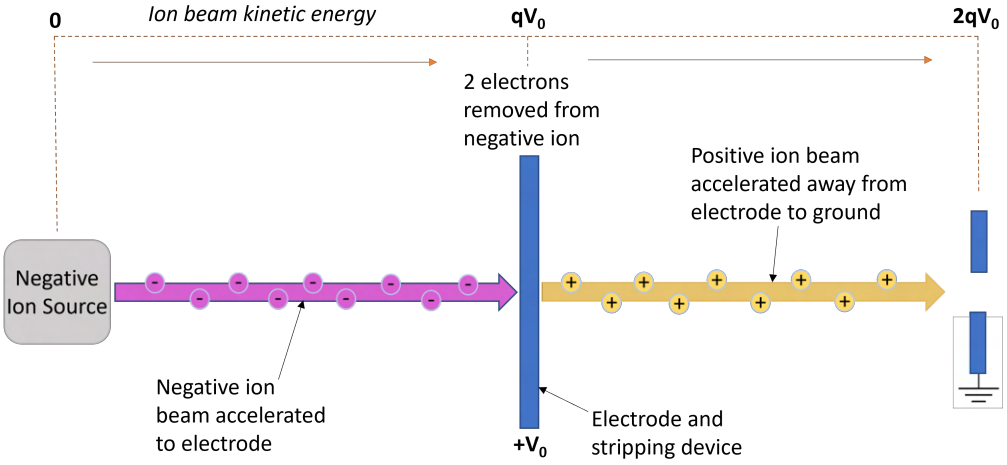

Figure 1.1: Diagram of tandem accelerator

The use of tandem accelerators allows ion beams to reach high energies without the need for pulsed acceleration. This method of acceleration is important in many industries and research areas such as surface analysis, which uses techniques like Rutherford Backscattering Spectrometry (RBS) and Particle Induced X-Ray Emission (PIXE) to determine the elemental composition of different materials [3]. Tandem accelerator are also useful in accelerator mass spectrometry (AMS) which is a common method for separating rare isotopes from a material [4]. A widely used industrial application of negative ion beams leveraging tandem accelerators is ion implantation for semiconductor devices [5]. Ion implantation is a multi-billion dollar industry that uses ion beams to change the doping profile of different semiconductors in order to create precisely tuned micro-electronic devices [6]. Typical negative ion beams used for this application are boron, arsenic and phosphorus [7], but, high energy light ions such as hydrogen and helium are implanted in power electronic devices for improved capabilities related to the switching response

and breakdown voltages of the resulting transistor products [8]. A common method for producing the negative ions used for this application is through a charge transfer with an alkali or alkaline earth metal vapour [9]. In this method, positive (1+) ions are passed through a vacuum region, with injected metallic vapour, at an energy of a few tens of keV where a collision takes place between the incident beam and the vapour target [10]. During these collisions, two electrons are transferred from the alkali or alkaline earth metal atoms onto the incident positive (1+) beam to form a negative (1-) ion beam of the same species which is extracted from the charge transfer region [11]. The issue with this technique for negative ion production is that the metallic vapours used for charge exchange can cause contamination issues in the implanter systems. The vapours have been known to transport through the system and deposit onto the semiconductor devices causing detrimental impurities and rejected devices. These vapours can also coat vacuum surfaces causing arcing or shorting issues in electrostatic components and can pose difficult maintenance issues as they are combustible substances [12]. If these negative ions can be formed without using a metallic vapour medium it would eliminate the contamination and maintenance issues associated with this particular method of ion production. Negative ions such as helium are almost exclusively formed using the charge transfer process described above [13]. For this project it will be explored to see if negative ions can be formed by using D-Pace's TRIUMF licensed volume-cusp H^- ion source [14] to create negative ions through charge exchange. An incident H^- beam will be passed into a vacuum region of inert non-metallic gas in an attempt to transfer the extra electron from the hydrogen beam onto the target gas. Due to the important commercial applications of producing negative helium ions without metallic vapour contamination, helium was chosen as the first target to study. The hypothesized general charge transfer reaction is shown in equation 1.1.

$$H^- + He \rightarrow H + He^- \tag{1.1}$$

Different readily available non-metallic, non-toxic gases will be studied after helium is thoroughly explored as a target option. The other targets may not have known commercial applications but will give novel measurements for their collision with an incident H^- beam under the given conditions. After a potentially successful electron transfer from the incident H^- beam, the resulting negative ion beams will be accelerated by an in-vacuo electrostatic accelerator and the resulting beams will be differentiated using a mass spectrometer system. Figure 1.2 shows a basic diagram of the experimental setup and the ion beam transport and creation throughout the system using the helium target gas as an example. The experimental setup will be descried in greater detail in Chapter 3. Note that the energies associated with the ion beams in figure 1.2 are example values and can be adjusted.

This method follows an example set by Doupé and Litherland [15] where a negative copper ion beam (Cu^-) was incident on inert ICl gas to produce the following collisional reaction: $Cu^- + ICl \rightarrow Cu + ICl^{-*} \rightarrow Cu + I + Cl^-$. This charge transfer process of negative beams incident on neutral gases has not been extensively studied compared to the negative (1-) ion beam production from positive (1+) ions, but it has been explored by a few researchers. Groups such as Bailey and Mahadevan [16], Hasted and Smith [17], Muschlitz [18], Bardsley [19], Gupta and Melton [20], and Esaulov et. al. [21] have all studied the electron detachment from negative ion beams due to collisions with different inert gas targets and have measured the cross-section of any charge exchange through the

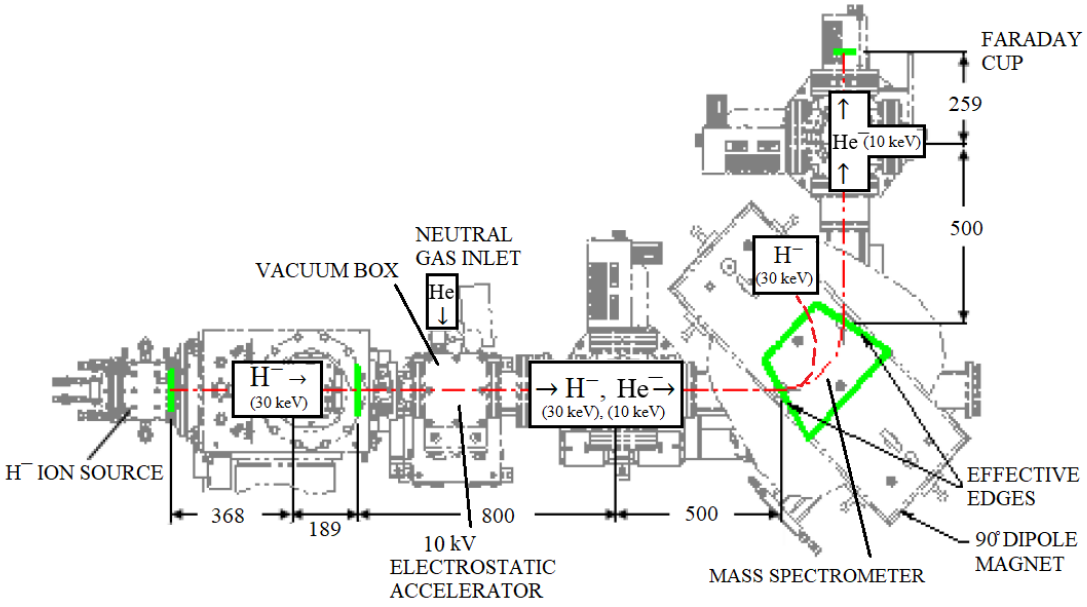

Figure 1.2: Overview of experimental setup and ion beam path (all measurements in mm)

nature of the electron detachment and measure of the electrons emitted from the collisions. None of these experiments reported the production of negative helium ions. Apart from Doupé and Litherland, it is not known that there have been any other attempts to re-accelerate these negative ion beams that are formed through collision with incident negative beams as a way of measuring conversion efficiency. Thus, this project presents a novel innovative technique for the production of negative ions that has never been explored.

This thesis will study the interaction between H^- ion beams at tens of keV on non-metallic neutral gases. An attempt to accelerate and measure any newly produced negative ion beams using this inventive new technique will be made and the any resulting conversion efficiencies will be recorded. The interaction between the H^- ion beams and different neutral, non-metallic, non-toxic gases He, H_2, CO_2, and O_2 will be studied with the goal of creating negative ion beams in a charge transfer cell that can be accelerated and detected. The magnitude of any resulting negative ion beam current values will be reported.

The following list is a road-map of the thesis and what will be included throughout.

1. Chapter 1 discusses the relevance and motivation of the research which is pursued and a brief summary of the previous research performed in this area of study.

2. Chapter 2 goes through background theory of relevant topics associated with this study, largely focusing on negative ion formation and mass separation which will be important in understanding the experimental method and explaining results.

3. Chapter 3 gives a detailed description of the experimental setup and the design work that went into the construction of the charge exchange cell which includes an electrostatic accelerator and custom removable Faraday cup.

4. Chapter 4 presents the method in which the H^- collision experiments were performed as well as the respective results.

5. Chapter 5 summarizes the findings of this thesis and the lessons learned from exploring the field of charge exchange as well as future work which could be performed to further investigate this topic.

Throughout the duration of this thesis project I conducted a thorough literature research on charge exchange ion sources and relevant theory. Using the knowledge gained from this research I worked on the development of a novel method for producing negative ions through charge transfer. I designed, manufactured, constructed, and tested a charge exchange gas cell which included an electrostatic accelerator and a custom Faraday cup for beam current measurement. I also developed controls programs to easily adjust the experimental parameters of the test setup. I learned how to operate D-Pace's Ion Source Test Facility which included tuning the TRIUMF licenced H^- ion source which was used as the driver for the experiment. I developed a vacuum system simulation for the beamline of the experimental setup in order to approximate the pressure of the system in regions which did not contain vacuum gauges. I then conducted numerous experiments using multiple gas targets (He, H_2, CO_2, O_2) in order to test the novel method for negative ion formation using the H^- ion source driver. I made numerous modifications to the gas cell/electrostatic accelerator in order to make them more robust and suited for high beam power experiments. Finally, I compiled the data gathered and developed theories for the interesting results found.

Chapter 2

Negative ion formation

2.1 Ion sources

Ion sources are classified as devices that produce extracted beams of ions [9]. Most are composed of two main components, the plasma source and the extractor. The plasma source is a region where electrons, neutrals, positive ions and negative ions are formed and confined. The desired ions are extracted from the plasma source using a series of lenses with different potentials in order to focus the ion beam and filter out any electrons or unwanted ions. A basic image of a simple ion source is shown in the image below.

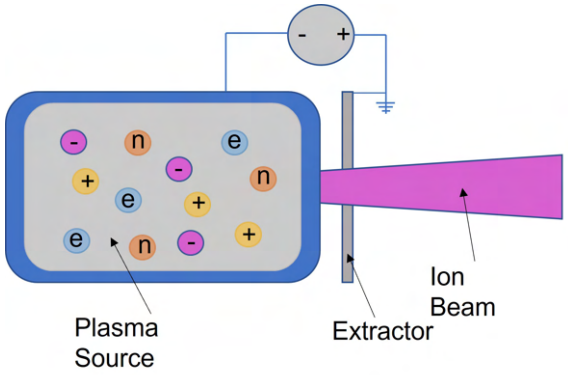

Figure 2.1: Basic diagram of a negative ion source

Ion sources are typically named based on the method in which ions are formed in the plasma. Examples of common ion formation techniques are, electron impact ionization, photoionization, field ionization, surface ionization, and ion impact or charge exchange ionization [9]. The parameters of these plasmas are crucial to the effective formation of ions, the two most basic characteristics being the temperature and density of the plasma [22]. In general, plasmas are quasi-neutral meaning that the overall charge of the plasma at any given time is approximately neutral. If we consider particles with different charges Q_j (...-2, -1, 0, +1, +2...), and different densities for all particles species in the plasma n_j (electrons-n_e, ions-n_i, neutrals-n_n) then the following expression gives a general condition for a plasma [22].

$$\sum Q_j n_j = 0 \tag{2.1}$$

2.2 Charge exchange

Negative ions sources are typically classified by three different source types; surface production, volume production, and charge exchange. Surface production sources rely on electron transfer from the conduction band of a metal surface. Volume production sources utilize the attachment of electrons from a plasma to the prospective negative ion species. Negative ions produced from charge exchange ion sources gain electrons through free particles such as free electrons, gas atoms or molecules, or metallic vapours [11]. Traditionally, charge exchange negative ion sources leverage a positive ion source in order to pass a positive ion beam (Y^+) through a target vapour (X), in order to produce the following conversion [23].

$$\begin{aligned} Y^+ + X &\rightarrow Y + X^+ + \Delta E_1 \\ Y + X &\rightarrow Y^- + X^+ + \Delta E_2 \end{aligned} \tag{2.2}$$

The negative ions are thus produced by a two-step charge exchange where positive ions gain two electrons from the target vapour by two different collisions. The ΔE components of the reactions shown in equation 2.2 represent the energies produced, or required, for the charge transfer to be complete, this is also known as the mass (or energy) defect of the collision. The mass defect is simply the change in energy states for both the projectile and target summed together.

$$\begin{aligned} \Delta E_1 = E(Y^+) + E(X) - E(Y) - E(X^+) \\ \Delta E_1 = E_i(Y) - E_i(X) \\ \Delta E_2 = E(Y) + E(X) - E(Y^-) - E(X^+) \\ \Delta E_2 = E_A(Y) - E_i(X) \end{aligned} \tag{2.3}$$

The difference in energy between positive ions and their ground states equates to the ionization energy (E_i) of that species whereas the difference in energy between a negative ion and its ground state is the electron affinity (E_A) of the species. In general, a mass defect close to zero results in an increased cross-section and a much higher probability of charge exchange [24]. The charge transfer between an ion and target atom/molecule is classified as being either resonant or non-resonant. Resonant charge transfer occurs when the projectile (Y) and the target (X) are the same species at their ground states, hence a mass defect ΔE_1 of zero and a high probability for charge transfer. Non-resonant charge transfer occurs when the projectile (Y) and target (X) are different species resulting in a non-zero mass defect value ΔE_1. The cross-sections for non-resonant charge transfer can be extremely small if the mass defect values for the collision are too large. In the case of equation 2.2, if $Y = X$ a resonant charge exchange would occur for the neutralization in the first step of the reaction, which would have a very large cross-section. However, negatively ionizing the projectile in the second step of the reaction would not yield a large cross-section as the mass defect ΔE_2 takes the difference between the electron affinity and ionization energy. This collision would result in a much smaller cross-section as these values would be inherently different. Therefore, optimal production of negative ions using this method is carried out with different species that will minimize the mass defects for both steps in the charge exchange process, this is called near-resonant charge exchange [25] and is classified as a charge exchange reaction with a mass defect less than 1 eV [26]. It should be noted that for near and non-resonant reactions, the impact speed of

the projectile ion greatly effects the cross-section of the interaction. Massey proposed that for certain reactions if the projectile is approaching the target slowly the internal motion of the target's state is able to adjust so that an electronic transition doesn't take place [26]. This projectile speed range which forbids charge transfer is called the "adiabatic region". The conditions for this adiabatic region as hypothesized by Massey are outlined by equation 2.4.

$$\frac{a|\Delta E|}{hv} \gg 1 \tag{2.4}$$

The arguments of equation 2.4 are as follows; a is the "adiabatic parameter" which is defined as the effective distance at which interactive forces act between the colliding particles, ΔE is the mass defect of the prospective charge transfer, h is Planck's constant, and v is the relative velocity of the incident particle. Other researchers such as Fogel [27] and Grüebler [28] have explored the optimal incident particle velocity in which the cross-section of the charge exchange collision for different particles is maximized. From Massey's criterion, they have proposed that the optimal incident particle velocity v_{max} is reached when equation 2.4 approximately evaluates to 1.

$$\frac{a|\Delta E|}{hv_{max}} \simeq 1 \tag{2.5}$$

The experimental results from this prediction somewhat agree with the criterion but it is seen as more of a guideline for effective charge transfer. In the case of charge exchange from an incident negative ion onto a neutral vapour target, such as the single-step charge exchange outlined by Doupé and Litherland [15], the mass defect of the reaction is minimized (cross-section is maximized) when the electron affinities of the projectile and target are similar. The calculation of ΔE is outlined in equation 2.6.

$$\begin{gathered} Y^- + X \rightarrow Y + X^- + \Delta E \\ \Delta E = E(Y^-) - E(Y) + E(X) - E(X^-) \\ \Delta E = E_A(X) - E_A(Y) \end{gathered} \tag{2.6}$$

From this sub-section, it can be gathered that it is important that both the mass defect of the collision is minimized and the projectile has a velocity that is outside of the adiabatic region.

2.2.1 Example: He^- production

A negative ion which is commonly formed using a charge exchange ion source is the metastable negative helium ion He^-. He^+ ions (Y) are passed through an alkali or alkaline-earth metal vapour target (X) to form He^- as in equation 2.2. An important detail about this transition is that the intermediate neutral He is not in the ground state $(1s^2)^1S$ but is in an excited triplet state of helium $(1s2s)^3S$ which has an energy of 19.77 eV [24]. This metastable state of helium has a positive electron affinity of 0.0774 eV which allows for the formation of a metastable negative ion $(1s2s2p)^4P$ [29]. Since helium is the projectile, and the energy level of He^+ is 24.6 eV, from the ground state [30], the value of $E_i(Y)$ in equation 2.3 is 4.8 eV. The ionization energy range of alkali metals ($E_i(X)$) is between 3.89 eV and 5.39 eV [24] which would result in an energy defect ΔE_1 (eqn. 2.3) no greater than 0.91 eV, this would be classified as a near-resonant transition. As for the second transition from neutral energetic He to He^-, the energy defect ΔE_2

takes the difference between the electron affinity of He (0.08 eV) and the ionization energy of the alkali target ($E_i(X)$). This value would equate to 4-5 eV, but, for this system, it is theorized by Main that a Coulomb interaction factor must be accounted for which happens to have a value of a few eV creating a near-resonant charge transfer [24]. It has been outlined by Hasted and Lee [31], and Grüebler [28], that the value of ΔE is actually a composition of different integrative forces which are largely dependent on the type of collision. A breakdown of the mass defect is shown in equation 2.7.

$$\Delta E = \Delta E_\infty - E_c - E_p - E_x \tag{2.7}$$

ΔE_∞ is the mass defect for infinite Coulomb separation which is commonly the dominating value of calculation for mass defect and is governed by the changes in energy of the projectile and targets from the collision as outlined in equations 2.3 and 2.6. E_c is the coulomb interaction which has a significant value in the experiments performed by Main [24] as described above but is typically not reported in other experiments focusing on minimizing mass defects for increased cross-sections for charge exchange. E_p is the polarization interaction of the species, while E_x is the excitation energy of the reaction products. It should be noted that Hasted and Lee consider a screen interaction E_{SC} as part of the mass defect arguments instead of the excitation energy, this discrepancy is not well defined but both terms seem to be negligible in calculations carried out in the literature. Considering this definition of the calculation of the mass defect for negative helium production, the alkali medium allows for near-resonant charge transfer for both collisions and will produce a large cross-section and a relatively high conversion rate for the overall reaction. Figure 2.2 shows the different energy states of helium and the transitions which are possible from one state to another.

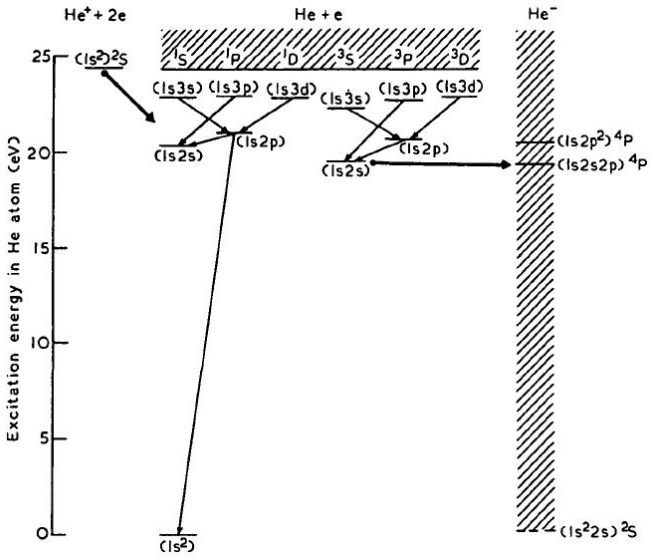

Figure 2.2: Transitional states of helium and their corresponding energy levels for a double charge transfer reaction [24].

Figure 2.2 shows all the states of He^+ ions, neutral helium states, and He^- ions. The notation of these states refers to the location of the electrons and whether the electrons are configured in a singlet, doublet, or triplet state. For example, $(1s2s)^3S$ tells us that one electron is in the ground (1s) shell, the other electron is in the valence (2s) shell, and they are oriented in a triplet configuration with both electrons in the S subshell. Triplet,

refers to the electrons having a parallel quantum spin (S = 1), whereas singlet refers to the paired electrons having an anti-parallel spin (S = 0) and a doublet states that there is an unpaired electron in the configuration [32].

In order to understand the meaning behind the particle energies when explaining charge exchange ion sources, a brief description of important concepts in charged particle dynamics will be discussed.

2.3 Charged particle beam energy

The rest energy of an object E_0 is described through the mass-energy equivalence which was developed and proposed as a general principle by Albert Einstein.

$$E_0 = mc^2 \tag{2.8}$$

This energy is considered to be the total energy of the object or system when it is not in motion in it's frame of reference [33]. When an object is in motion, the total energy is a summation of the rest energy and the object's kinetic energy.

$$E_{tot} = E_0 + E_{kin} \tag{2.9}$$

It is common in the field of accelerator physics to refer the kinetic energy of a charged particle beam simply as the "energy", this is not to be confused with the total energy of the particles. Another common theme in accelerator physics is to use units of electron-volts (1 eV = 1.602×10^{-19} Joules). These units of eV are typically accompanied by the speed of light (c) when dealing with values of mass and momentum, for example, when dealing with values of mass 1 MeV/c^2 = 1.79×10^{-30} kg, and 1 MeV/c = 5.36×10^{-22} kg m/s when working with momentum. It should be noted that when an object's speed v approaches the speed of light, the mass of the particle increases and the kinetic energy is determined by scaling the rest energy using the Lorentz factor γ.

$$\gamma = \frac{1}{\sqrt{1-\frac{v^2}{c^2}}} \tag{2.10}$$

$$E_{kin} = (\gamma - 1)mc^2 \tag{2.11}$$

The momentum of an object p is determined by the energy-momentum relationship outlined in equation 2.12 [40].

$$pc = \sqrt{E_{tot}^2 - E_0^2} \tag{2.12}$$

Using the relations given in this section one can determine the momentum and total energy of a charged particle beam given the kinetic energy and particle species.

It is important that charged particle beams are well focused when being directed towards targets for charge exchange in order to produce high conversion rates. In the next sub-section, ion optics are discussed to explain ion beam steering and manipulation.

2.4 Ion Optics

Ion beams are manipulated by electric and magnetic fields seeing as they are charged particles and are subject to electric and magnetic forces. Electric fields can be used to accelerate, focus, and steer beams, whereas magnetic fields are only able to focus and steer. The magnetic force on a charged particle acts perpendicular to the direction of motion and thus can only steer or focus and not accelerate. This is made clear through equation 2.13 where the magnetic force is calculated by a cross-product between the magnetic field and velocity of the particle.

$$\mathbf{F} = q(\mathbf{v} \times \mathbf{B}) \tag{2.13}$$

The force acting on a charged particle from an electric field is calculated using equation 2.14.

$$\mathbf{F} = q\mathbf{E} \tag{2.14}$$

Clearly, the force from an electric field is independent of the direction of motion of the particle. Thus, electric fields can be used for both acceleration and steering/focusing. This being said, electric fields are only a good steering/focusing option when low energy particles are considered. For example, a 1 MeV beam of protons requires a magnetic field strength of 0.14 T in order to be bent by 90° over a 1 m distance which is a very reasonable value for commonly sourced permanent and electromagnets. However, an electric field strength of 1.94 MV/m would be required to achieve the same force, which is an unreasonable potential to obtain over a distance of 1 m with common power supplies. Thus, electric fields are typically used for acceleration and magnetic fields used for focusing and steering. Particle beam acceleration is performed using many different techniques and is typically grouped into two categories, Direct Current (DC) acceleration and Radio Frequency (RF) acceleration. RF acceleration uses RF waves to distribute and shift electromagnetic fields to accelerating cavities or electrodes [34]. The main advantage to RF acceleration is that they are capable of providing the same amplitude of acceleration to a particle many times over the course of transport to create higher energy beams and are not limited by the maximum capabilities of a voltage generator. However, this form of acceleration can only yield bunches of particles and is incapable of providing a consistent stream of beam due to the wave nature of the frequencies used for electromagnetic modulation. DC acceleration is much simpler in that it uses a fixed electric field provided by a direct current voltage generator to accelerate particles from one electrode to another. The disadvantage to this form of acceleration is that the particle beam energy is greatly limited by the potential provided by the voltage generator. Equation 2.15 gives the equation for the energy of a particle with charge q passing through a single-ended electrostatic accelerator over a potential V.

$$E = qV \tag{2.15}$$

Common DC generators only reach tens to hundreds of kV and sophisticated generators reach a maximum around a few MV [35], thus, these energies are limited to low MeV ranges. Therefore, it is more practical to use electrostatic accelerators for applications which require non-bunched constant low energy beams.

Electrostatic accelerators use different types of accelerating lenses such as tube lenses and aperture lenses. Tube lenses allow for drift periods within the lens and have a focusing effect on the exit of the lens and a defocusing effect on the entrance of the lens [35]. Aperture lenses are thin conducting plates with an aperture for particle transport, the plates are set at different potentials that create an electric field between lenses. Given two electric field gradients E_1 and E_2 where E_2 is further downstream of E_1, the lenses are accelerating and focusing if $E_2 > E_1$ and decelerating and defocusing if $E_2 < E_1$ [35].

The next few sub-subsections give an explanation of some key concepts which are integral in the understanding of particle beam optics.

2.4.1 Emittance and brightness

The emittance of a beam is a very important specification and refers to the particle beams "size" in a phase space. The phase space is a two dimensional space which spans the physical position of the particle in the beam on one axis with respect to it's momentum in that axis. We are typically interested in the "x" and "y" emmitance of a beam if the particle is travelling in the "z" direction. This information tells whether the beam is converging or diverging, and how much physical space the beam occupies in the "x-y" plane. In terms of optics, a beam with smaller emittance value is more desirable as it would occupy a smaller physical space and have a smaller variation in size as it travels through a beamline. This would allow the beam to be passed through apertures in a beam line with little loss. It should be noted that the total emmitance of a beam is conserved and that focusing a beam only reduces the emittance in one plane, thus, increasing the emmitance value in the transverse plane. The emittance of a beam is ultimately minimized at the source of the particle beam.[36] Figure 2.3 shows an example of a phase space ellipse, this is the effective area in the position-momentum plane and is, by definition, the emmitance value.

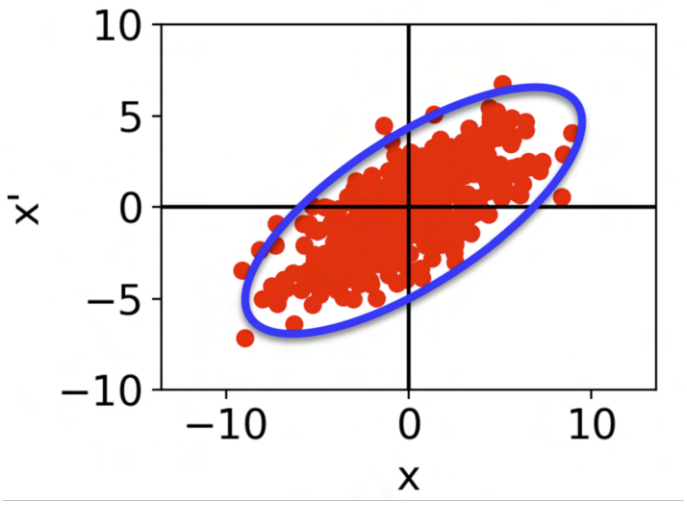

Figure 2.3: An example of a diverging beam ellipse in the x-axis. The units of this plot are arbitrary. [37].

In addition to emittance, the brightness of a particle beam is also an important metric which gives quantitative value to the quality of the beam. The brightness of a beam (B) is related to the the emmitance (ε) through the beam current (I) and wavelength of the associated particles (λ) through equation 2.16.

$$B = \frac{I}{\lambda \varepsilon} \tag{2.16}$$

Thus, to increase the quality of the beam based on the measurement of brightness, beam current must be maximized and emmitance must be minimized. [36]

2.4.2 Space charge and perveance

On the topic of beam quality, it is important to to have an understanding of self-fields such as space charge which can cause detrimental beam degradation through mechanisms like energy loss, phase, and frequency shift. Space charge is a phenomena which is seen in particle beams that can be explained through the Coulomb force and the magnetic force produced by a current. If particles of the same charge are travelling in one direction in a confined space (a beam), the particles will be repelled by by the Coulomb force, but, they will also be attracted by the magnetic fields induced through the current they produce. Ultimately, the Coulomb force is dominating unless the particles are moving at the speed of light (in which the forces cancel) [38]. On the topic of charge exchange ion sources, the space charge effect can be combated by injected gas in the area of beam formation, this causes ionization of opposing charged particles which would attract the particles of the objective ion beam to the beam center, reducing the emittance. The effect that space charge has on a charged particle beam can be quantified using a value called perveance. Perveance (P) of an electron beam can be calculated by the beam current (I) and energy (U) in equation 2.17.

$$P = \frac{I}{U^{3/2}} \tag{2.17}$$

Thus, a low energy beam would have a high perveance value and a greater space charge effect and can benefit from the injection of residual gas to produce a higher quality beam.

The next sub-section will explain the concept of mass spectrometry which is used to differentiate ion beams formed with different masses and energies.

2.5 Mass spectrometry

In a charge exchange ion source many different negative and positive ions can be formed depending on the target vapour and the primary incident beam species [39]. In order to differentiate the extracted beams from one another, the beams are bent using an electrostatic or magnetic force. Electrostatic forces are used to bend low energy, light particles like electrons, whereas magnetic forces are used to bend larger or higher energy particles. If two particle beams possess the same energy, they are differentiated by their mass. In the case of magnetic fields being used to alter the path of charged particles for mass separation, a dipole can be used to bend the particles on one plane since the magnetic force is perpendicular to the particle trajectory. If a particle beam is passing through a dipole magnet with the particle trajectory perpendicular to the magnetic field direction then the magnetic force will always be perpendicular to the particle trajectory. As a result, it can be said that the centripetal force is equal to the magnetic force acting on the particle beam which results in the following expression.

$$B\rho = \frac{p}{q} \tag{2.18}$$

This relation is commonly referred to as magnetic or beam rigidity [40], since the beam momentum p is proportional to the magnetic field strength B and the bending radius ρ, thus a beam with a larger momentum is more "rigid" (i.e. the particle trajectory is more resistant to change in direction due to magnetic force). It should also be noted that the magnetic field strength and bending radius are inversely proportional to the charge of the particle q. If an electromagnet is used, the polarity of the magnet (magnetic field direction) can be used to differentiate positive and negative ions, whereas the strength of the magnetic field is used to separate ions with different energies and masses. Different isolated detectors located in an array of positions may be used to measure different particle species and energies if the particle beams are passed through a permanent magnet.

If a dipole electromagnet is used for ion separation, the strength of the magnetic field is varied by changing the current passing through the coils (I) which are used for the magnetic poles. If the current required to bend an incident particle beam I_X, of mass m_X, about a fixed radius R, at a energy E_X, then the current required to detect a different particle beam I_Y about the same radius can be easily scaled given the secondary particle mass m_Y and energy E_Y. The magnetic force on a charged particle moving through a dipole magnet on a plane parallel to the faces of the poles will always act perpendicular to the direction of the particle, thus, the magnetic force equates to the following:

$$F = qvB \tag{2.19}$$

Since the force acting upon the charged particle beam will result in a uniform motion of curvature, this magnetic force is equal to the centripetal force.

$$F = qvB = \frac{mv^2}{R} \tag{2.20}$$

For non-relativistic particle beams, the classical kinetic energy of the beam ($E = \frac{1}{2}mv^2$) can be substituted into the force equation in order to display relation in terms of the known energy and mass values.

$$q\sqrt{\frac{2E}{m}}B = \frac{2E}{R} \tag{2.21}$$

Rearranging equation 2.21 gives an expression for magnetic field strength in terms of particle energy, mass, and charge over a set radius R.

$$B = \frac{1}{q}\frac{\sqrt{2Em}}{R} \tag{2.22}$$

Taking a ratio of equation 2.22 for two different particles (X and Y) travelling over the same radius R produces the following expression:

$$B_Y = \frac{q_X}{q_Y}B_X\sqrt{\frac{E_Y m_Y}{E_X m_X}} \tag{2.23}$$

The magnetic field strength in the center of a current carrying loop of fixed radius r is given by:

$$B = \frac{\mu_0 I}{2r} \tag{2.24}$$

Since the radius of the current carrying coils in the electromagnet will not vary in size, the magnetic field strength values in equation 2.23 are linearly proportional to their respective current values (I_X and I_Y).

$$I_Y = \frac{q_X}{q_Y} I_X \sqrt{\frac{E_Y m_Y}{E_X m_X}} \tag{2.25}$$

Thus, if both particle beam species X and Y have a known energy, mass, and charge, the current in which the particle beam Y can be detected by the mass spectrometer system (I_Y) can be calculated if the current at which the particle beam X is detected is known (I_X).

In order for these ion beams to travel through a beamline to a detector without disruption, an evacuated path must exist with few particle obstructions. The basic theory of vacuum physics is explained in the next sub-section in order to give an understanding on how to achieve this evacuated beamline.

2.6 Vacuum physics

The word vacuum is derived from the Latin word "vacua" meaning "empty" [41], although, in practice, a truly empty space is not achievable and regions can only be partially evacuated. In a practical sense, vacuum is described as a region of space with pressures lower than atmosphere at a constant temperature. The pressure of a system p is simply calculated by the force F acting on some surface area A.

$$p = F/A \tag{2.26}$$

The standard units of pressure are Pascals (Pa), where 1 Pa = 1 N/m^2, and atmospheric pressure is defined as 101,325 Pa at sea level. Other units of the measure of pressure include mbar and Torr, where 1 Pa = 0.01 mbar = 0.0075 Torr. Different levels of vacuum are classified by pressure ranges, these ranges are shown in table 2.1.

Table 2.1: Vacuum levels and respective pressure ranges [41].

Vacuum Range	Pressure Range (mbar)	Pressure Range (Torr)
Low (LV)	$3.3 \times 10 - 1 \times 10^3$	$25 - 750$
Medium (MV)	$1 \times 10^{-3} - 3.3 \times 10$	$7.5 \times 10^{-4} - 25$
High (HV)	$1 \times 10^{-6} - 1 \times 10^{-3}$	$7.5 \times 10^{-7} - 7.5 \times 10^{-4}$
Very High (VHV)	$1 \times 10^{-9} - 1 \times 10^{-6}$	$7.5 \times 10^{-10} - 7.5 \times 10^{-7}$
Ultra-High (UHV)	$1 \times 10^{-12} - 1 \times 10^{-9}$	$7.5 \times 10^{-13} - 7.5 \times 10^{-10}$
Extreme Ultra-High (XUHV)	$\leq 1 \times 10^{-12}$	$\leq 7.5 \times 10^{-13}$

Vacuum is achieved by pumping out particles from a confined space. There are many different pumping techniques which are used to reach different levels of vacuum, for example, positive displacement pumps use mechanical movements to push volumes of gas out of a region with synchronized valve systems to create partial pressures in the LV to MV pressure regions. More sophisticated mechanical pumps, known as momentum transfer pumps, are used to create HV and sometimes VHV vacuum environments by directing

the particles out of region of interest by collision with fast moving blades or rotors. Creating vacuum environments that have pressures in the UHV and XUHV regions require capture pumps, where the particles are actually implanted or trapped into a solid material which is part of the pump. These capture pumps commonly ionize the particles in order to permanently contain them using electric and magnetic fields [42]. The gauges used to measure vacuum pressures are typically classified as directly measuring and indirectly measuring vacuum gauges. Directly measuring vacuum gauges use mechanical systems to calculate the force acting on a surface which gives the pressure of the system. These gauges are typically used for measuring low or medium vacuum ranges and are incapable of accurately measuring high vacuum environments as the forces acting on the vacuum surfaces become too small to record [43]. Indirectly measuring vacuum gauges use properties of gases which are proportional to the number of particles in a region to determine the pressure of a system. Certain gauges such as ion and cross field gauges use conducting plates to measure either the ionization rate or discharge current between the plates to calculate the pressure of the system as these properties are proportional to the number of molecules in the system [44]. Indirectly measuring gauges are commonly used for measuring pressure in the HV to XUHV regions.

Sometimes high pressure environments are introduced into a vacuum system in order to create collisions between charged particle beams and target gases. When analyzing particle collisions it is important to have an understanding of the cross-section of the collision. The cross-section will be explained in the following chapter sub-section.

2.7 Cross-section

When discussing particle collisions in physics, in a general sense, the cross-section refers to the probability of a collision between particles and is represented by an effective area [45]. Cross-sections for the collision of particles are dependent on the the incident particles beam flux (I), the density of target particles in the collisional region (n), the length of the region with a density n (dx), and the size of the particles colliding. The cross-section is also largely dependent on the incident beam energy and environmental aspects such as the temperature of the collision region. The cross-section is usually denoted by the symbol σ and has the units cm^2, so, the fraction of incident particles interacting with the target (dI) can be calculated. If the incident beam flux I has units of particles/s/cm^2, n has units of atoms/cm^3 and the length of the target is measured in cm the value dI can be found by equation 2.27.

$$dI = -In\sigma dx \tag{2.27}$$

This equation can be derived with respect to the position (x).

$$\frac{dI}{dx} = -In\sigma \tag{2.28}$$

This derivative has a general solution when the incident particles I have not passed through the target with length x and thus has a maximum value denoted by I_0.

$$I = I_0 e^{-n\sigma x} \tag{2.29}$$

There are many definitions of cross-sections depending on the interaction which is being discussed and thus different ways of predicting and measuring the cross-section of collisions. For charge exchange interactions it is the total electron loss cross-section (σ_{tel}) which is analyzed to determine a probability for charge transfer. The total electron cross-section is composed of the sum of three different electron detachment methods.

$$\sigma_{tel} = \sigma_s + \sigma_d + \sigma_c \tag{2.30}$$

From the components of equation 2.30 σ_s and σ_d represent the cross-section for single electron detachment and double electron detachment respectively. The single electron detachment cross-section σ_s, for most collisions, has been measured to be in the range of 10^{-15} cm^2 whereas σ_d is known to have the smallest values with a range of 10^{-16} to 10^{-17} cm^2 [46] [47]. The cross-section for electron loss through charge transfer is expressed by σ_c and is found to have the largest value when a resonant or near-resonant charge transfer takes place with values measured up to the 10^{-14} cm^2 range [15]. Thus, if a total electron cross-section in the range of 10^{-14} cm^2 is measured, it is likely that a resonant or near-resonant charge exchange has occurred between the projectile and the target. A typical method for measuring the total electron cross-section for charge exchange cells is to measure the current before and after the cell with a range of pressures and plot the data as $\ln(I/I_0)$ vs. pressure to take the linear slope of the trendline. The slope of these plots are used to find the cross-section σ_{tel} by rearranging equation 2.29.

$$\ln(I/I_0) = -n\sigma x \tag{2.31}$$

The density n can be expressed in terms of pressure P, temperature T and the Boltzmann constant k_B, so equation 2.31 becomes equation 2.32.

$$\ln(I/I_0) = -\frac{P}{k_B T}\sigma x \tag{2.32}$$

If the slope of the plot $\ln(I/I_0)/P$ is represented by m, the total electron cross-section is calculated by:

$$\sigma_{tel} = \frac{-mk_B T}{x} \tag{2.33}$$

Chapter 3

Ion Source Test Facility

3.1 System overview

The system used for all experiments associated with negative ion formation was an ion source test stand located at D-Pace, Inc. in Nelson, British Columbia. The test stand is equipped with a TRIUMF licensed, volume-cusp H^- ion source [14] that includes a pneumatic Faraday cup and an emittance scanner which are capable of intercepting the beam for diagnostic purposes. Downstream from the ion source there is a vacuum box that contains a charge exchange cell, which was designed, manufactured and assembled specifically for this project. Downstream of the charge exchange cell is the spectrometer system which is used for beam species separation. Finally, a 600 W fixed Faraday cup is located downstream of the mass spectrometer dipole in order to measure the current of any ion beams which pass through the mass spectrometer system. The following images show an overview of the Ion Source Test Facility (ISTF) and a labeled diagram highlighting key features including the components listed above.

Figure 3.1: Image of D-Pace ISTF taken from [48].

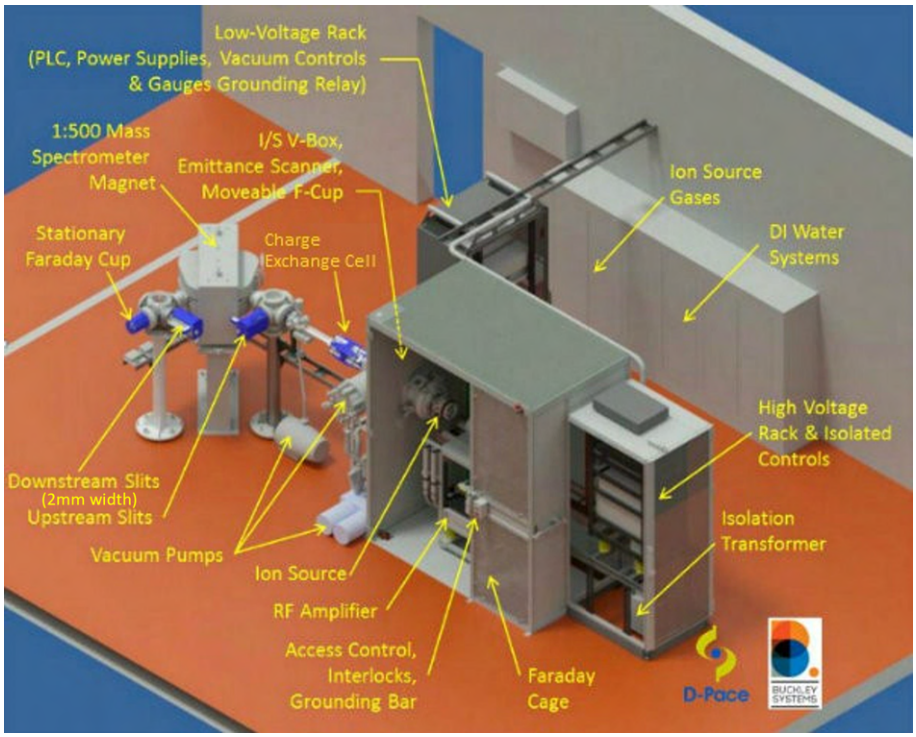

Figure 3.2: Labled diagram of D-Pace ISTF and key components taken from [48].

The proceeding sections of this chapter explain each major component of the ISTF and give a design overview for all components which were created specifically for this thesis. Explanation of conducted simulations which were performed in order to carry out both design aspects of components and mapping of vacuum pressures in the system are included. A brief description of a program which was modified to control the mass spectrometer power supply is also included.

3.2 H^- volume-cusp ion source

As mentioned previously, the driver ion source for the ISTF is a volume-cusp H^- source which is excited using a hot filament. This filament emits electrons (a few eV) which collide with the residual H_2 injected into the source to produce a high cross-section reaction called dissociative electron attachment (DEA) [10]. This reaction is displayed in equation 3.1.

$$H_2 + e \rightarrow H^- + H \tag{3.1}$$

The plasma is magnetically confined using a series of permanent magnets at different orientations. These ion sources are typically used as injectors for 30 MeV and 70 MeV cyclotrons used for medical radioisotope production and for tandem based Boron Neutron Capture Therapy. They can also be used for applications in fusion research and, as for this case, university research purposes. The H^- ion source can be tuned to operate at different energy ranges and beam currents. The stable energy range for a well focused beam is found to be between 15 keV and 30 keV, whereas the beam current can be adjusted from 0-15 mA. For more information on this ion source see the paper written by Kuo et. al. [14].

The following sub-section will include a description of charge exchange cell which was the primary focus in terms of development for this experimental setup.

3.3 Charge exchange cell: design, development, and implementation

The concept for the charge exchange cell used for this project was inspired by the design of Doupé and Litherland where gas was injected into a semi-contained region of the upstream side of an in-vacuo electrostatic accelerator [15]. A diagram of the electrostatic accelerator used for charge transfer in the experiments performed by Doupé and Litherland is shown in figure 3.3.

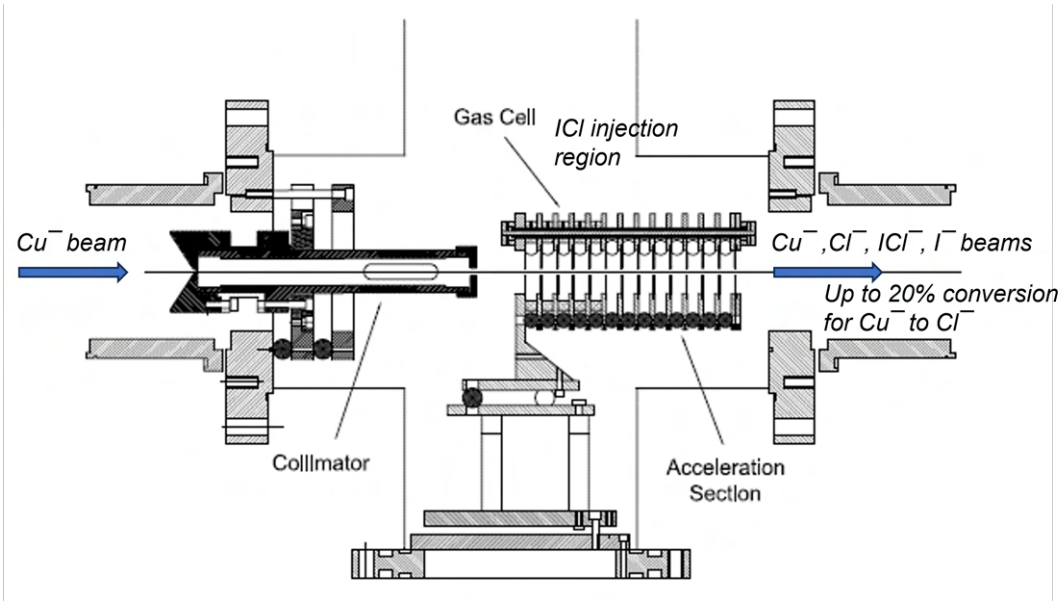

Figure 3.3: Diagram of electrostatic accelerator used for the production of Cl^- through charge exchange from an incident Cu^- beam in experiments performed by Doupé and Litherland [15].

The driver incident beam of H^- from the volume-cusp source is biased such that it is extracted by a grounded electrode, thus, in order to accelerate newly created negative beams, the incident beam must be slowed to some degree by the potential of the electrostatic accelerator. The impinged H^- beam should be collimated by a grounded plate with an aperture of a smaller diameter than the aperture of the accelerator. The accelerator, designed as part of this thesis work, consists of a series of electrode plates with apertures through the center for beam acceleration. The potential of each electrode increases towards ground so that the incident H^- beam is re-accelerated to its original energy and any new ion beams are accelerated to the potential difference between the position in which they were formed in the accelerator and the final ground electrode. The incident beam is slowed by the first electrode of the accelerator to an energy governed by the potential set by a DC power supply. The first four electrodes are isolated from each other with Teflon rings in order to create a semi-contained volume where non-metallic neutral gas can be injected. The length of the semi-contained region was based off the electrostatic

accelerator designed by Doupé and Litherland. Some preliminary experimentation was performed with differing lengths of this semi-contained region but did not produce any results to show that it increased the efficiency as no beam current was measured during this period. The remainder of the electrodes are isolated using ceramic stand-offs which allows the injected gas to disperse downstream of the primary collision point so that newly formed negative ions experience less electron loss through collisions with remaining inert gas. All electrodes are connected with a series of resistors to divide the voltage from the power supply amongst the electrode plates. A diagram of the general electrostatic accelerator design is shown in figure 3.4.

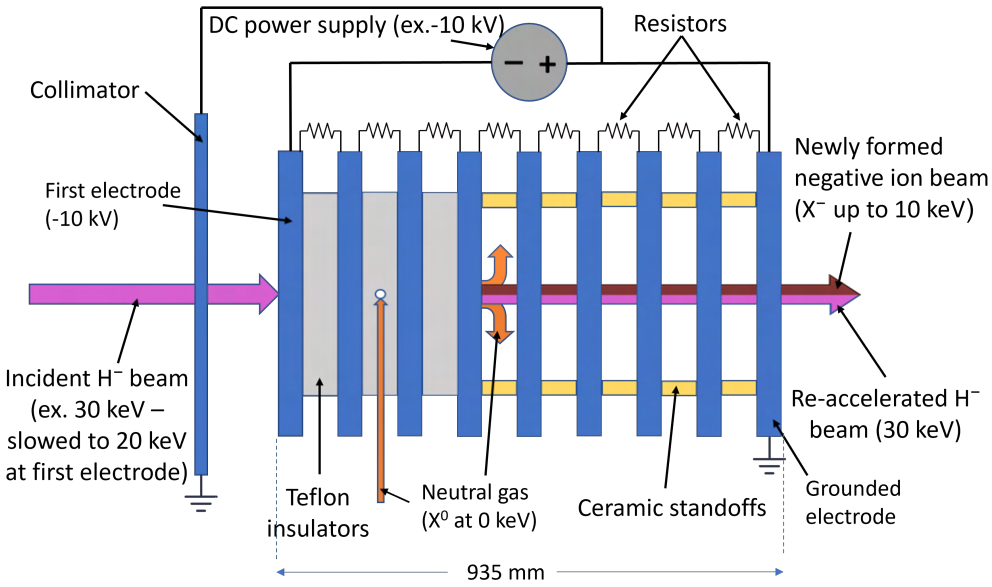

Figure 3.4: Diagram of novel gas cell/electrostatic accelerator schematic developed for this thesis project.

Since the beam energy is directly proportional to the potential which is applied to it ($E = qV$), the resulting energy of the newly created negative ion beams will be governed by the potential set by the DC power supply. For example, if a negative beam (1-) is newly created from the neutral gas target at the first electrode and the DC power supply is set to a value of -10 kV, the newly formed negative ions will have an energy with a magnitude of 10 keV once they have been accelerated to the grounded electrode. Also, the incident driver H^- beam is slowed by the electrostatic accelerator and then re-accelerated as it approaches the grounded electrode. For example, with a 30 keV incident H^- beam and -10 kV applied to the accelerator, the H^- beam will be slowed to an energy of 20 keV at the first electrode of the electrostatic accelerator and re-accelerated to 30 keV once it reaches the final grounded electrode. For simplicity, when the accelerator potential is referred to in this thesis, it will be the magnitude that is stated. The power supply is negatively biased and will only produce negative potential differences. An aperture lens approach was taken for electrostatic acceleration as a consideration for space within the available vacuum box in the beamline as the electrodes can be thin plates as opposed to longer accelerating tube lenses. This acceleration technique was also advantageous as the series of lenses can have a focusing effect when the magnitude of the electric field between plates increases throughout the beamline [35]. This increase in electric field gradient can be implemented by increasing the resistance value of the resistors between the electrodes.

This increasing electric field gradient also gives the advantage of reducing the energy spread of the resulting negative ion beams. If the difference in potential between the first few electrodes is not significant then the ions created within the semi-contained gas cell region will all be exposed to a similar acceleration from the electrode lenses. To keep the focusing effect of the lenses and reduce the energy spread of the prospective ion beams, a quadratic electric field gradient was chosen for the potential profile. The magnitude of the electric field strength between each electrode increases in a quadratic form until the ground electrode potential is reached at the last electrode. The first step was to determine how many electrodes would be able to fit in the vacuum box which was already integrated into the beamline of the ISTF. The number of electrodes is dependent on the gap between each electrode, this is dictated by the dielectric strength of the medium in between the lenses. It is known that the dielectric strength of air at atmosphere is 30 kV/cm [49], but the breakdown voltage between electrodes varies drastically with change in pressure, this is known as Paschen's Law [50]. Typically, the breakdown voltage reaches a minimum at a few hundred volts per cm at pressures between 10^{-1} to 10^{1} Torr [51]. Figure 3.5 shows the breakdown voltage of air as a function of pressure for a centimeter gap, this is known as the Paschen curve.

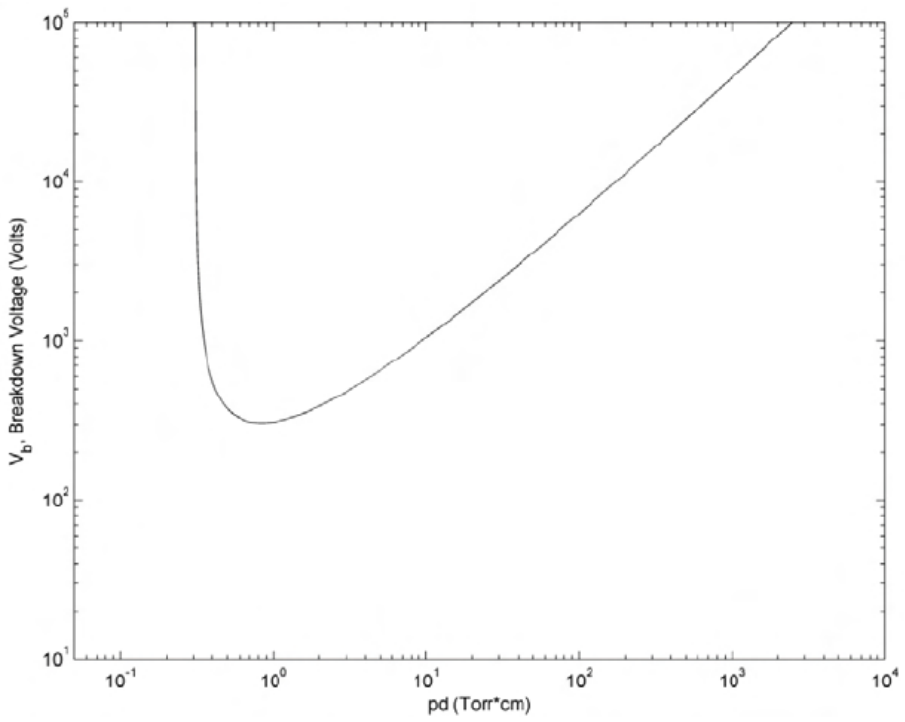

Figure 3.5: Paschen curve for air at 1 cm gap taken from [51]

The pressures achievable in the vacuum box where the electrostatic accelerator is placed in the ISTF during operation are between 10^{-6} Torr and 10^{-5} Torr. Thus, during regular volume-cusp ion source operation, potential gaps in the keV range are sufficiently insulated with air at the specified pressure range for cm distances. That being said, when inert gas is injected into the accelerator unit the pressure will rise in the semi-contained region of the accelerator. Beneficially and by design, with a quadratic electric field gradient applied to the accelerator, the electrodes which would see a higher pressure have a much smaller potential difference making the centimeter-range gaps sufficient for electric breakdown-voltage protection. Based on the available length of ceramic standoffs

used for electrode spacing, a 0.64 cm standoff was used for the electrode gaps and a 1.27 cm standoff was used for the collimator-first electrode gap. Recall that the collimator is grounded so the largest potential difference will be between the collimator and the first electrode. A thickness of 0.48 cm was set for the electrodes and collimator as this would be sufficient for attaching the resistors using M3 fasteners without overhang on the terminals, which would decrease the gap between electrodes at a localized point. Given that the total length of the vacuum box is 12.44 cm and the determined gap sizes, 9 electrode are able to fit in the space with a collimator. The diameter of electrodes were chosen such that gas inserts, resistors, and high voltage leads had clearance for attachment and that electrostatic breakdown would not be an issue between the electrodes and the walls of the vacuum box. Figure 3.6 shows the model of the electrostatic accelerator which was created using the online modelling software Onshape® [52].

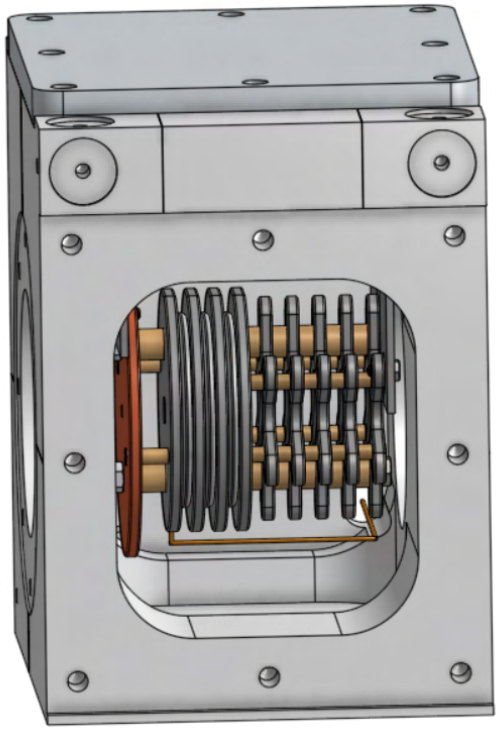

Figure 3.6: Onshape® model of electrostatic accelerator charge exchange cell placed in vacuum box.

It should be noted that the resistors will be mounted to the top of the electrodes in series in order to distribute the potential from the DC power supply. The electric field gradient was designed such that it would follow a quadratic path when comparing the potential of each electrode from the supply electrode to the ground electrode. Table 3.1 displays the potential values of each electrode if the upper limit of 20 kV is supplied to the accelerator from the DC power supply.

The quadratic electric field gradient was designed such that none of the resistors would go over their specified power rating. Of the resistors in question for the design, the lowest power rating was found to be 0.5 W. Based on the potential values shown in table 3.1, the largest magnitude of voltage between two electrodes was taken to be 5 kV. Thus, the maximum current flowing through the circuit was found to be 100 μA by Watt's law

Table 3.1: Designed electrode potential for a quadratic electric field accelerating gradient over 9 electrodes.

Electrode Number	Potential (kV)
1	20
2	19.7
3	18.8
4	17.2
5	15
6	12.2
7	8.8
8	4.7
9	0

($P = IV$). The total resistance of the circuit is found to be 200 MΩ through Ohm's law. In order to find the proper resistance value for each resistor bridging the gap between electrodes so that the quadratic potential field is created, the voltage is divided amongst the resistors using equation 3.2 [53].

$$V_1 = V_s \frac{R_1}{R_1 + R_2 + ... + R_i} \tag{3.2}$$

V_1 represents the voltage drop across the resistor being analyzed, V_s represents the value of the source voltage, and the R values are the resistances of the resistors in the series circuit; the denominator always equating to the total resistance (R_T) of the circuit (excluding the source resistance). Thus, the resistance of the resistor in question (R_a) can be calculated with the knowledge of the potential difference across said resistor (V_a) which can be easily calculated from table 3.1.

$$R_a = R_T \frac{V_a}{V_s} \tag{3.3}$$

Table 3.2 shows the resistance values for the 8 resistors which separate the electrode potentials. The resistor numbers are listed such that resistor 1 bridges electrode 1 and 2, resistor 2 bridges electrode 2 and 3, and so on.

Table 3.2: Theoretical resistor values for a quadratic electric field gradient in the accelerator with 9 electrodes.

Resistor number	Resistance (MΩ)
1	3.1
2	9.4
3	15.6
4	21.9
5	28.1
6	34.4
7	40.6
8	46.9

The material choice of the electrodes was based largely on the electrical conductivity, as the material should allow for charge to flow freely through the electrode in order to create a uniform electric field profile throughout the accelerator. Aluminum was chosen as the material for the electrodes as it has one of the highest electrical conductivity values of commonly used metals (60% of the conductivity of silver) and is easily machinable [54]. The concern with using aluminum for the collimator was that with a 5 mm aperture, if the incident beam is unfocused, most of the beam power will be dissipated into that material. Since the accelerator will be in a vacuum environment there will be no convective cooling and the collimator could potentially become too hot and jeopardize the integrity of the gas cell unit. Instead, a stainless steel collimator was manufactured as stainless steel possesses a melting temperature of 1510°C, compared to aluminum at 660°C [54]. High Density Polyethylene (HDPE) was originally chosen as the insulator material but this was later on changed to Teflon (PTFE) as the maximum operating temperature of PTFE is much higher than HDPE (260°C compared to 80°C respectively) [55]. The electrical insulation properties of PTFE are also more favourable than HDPE for this application, with the dielectric strength values being 50-170 kV/mm for PTFE and 22 kV/mm for HDPE. Once the material details were finalized, the electrodes and collimator drawings were sent out for manufacturing and the Teflon insulators were created using a CNC machine on site at D-Pace. The accelerator was aligned using an aluminum dowel with the same diameter as the electrode apertures with the end milled to the same diameter as aperture of the collimator. The accelerator was kept aligned and pressed together using ceramic rods which allowed for the central trajectory of the ions to stay consistent while maintaining isolation between the electrodes. A 1/32" hole was drilled through the side of the center Teflon insulator to allow for neutral gas injection. A gas feed-through was connected to the vacuum box through one of two available non-beamline vacuum ports. The other port was used for the high voltage feed-through which allows vacuum pressures to be maintained while delivering kV range potentials to the accelerator. The potential across the electrodes was tested at a lower voltage of 1 kV total from a DC power supply resulting in an overall current of 5 μA. Resistors with the exact values displayed in table 3.2 were not obtainable, thus, resistance values close to these numbers were chosen and are found in table 3.3 along with the resulting voltage drop across the resistor if 20 kV were applied to the accelerator.

Table 3.3: Actual resistor values used for the quadratic electric field gradient in the accelerator with 9 electrodes.

Resistor number	Resistance (MΩ)	Voltage drop (kV)
1	3.3	0.33
2	9.53	0.93
3	15	1.53
4	22	2.24
5	27	2.76
6	33	3.37
7	39	3.98
8	47	4.80

The accelerator was assembled and placed within the vacuum box using brackets that were created using aluminum sheets. The position and length of the brackets was deter-

mined using Onshape® so that the accelerator was inline with the center of the opening of the vacuum box and thus the center of the incident beam spot. Figure 3.7 shows the assembled gas cell placed in the vacuum box within the beamline.

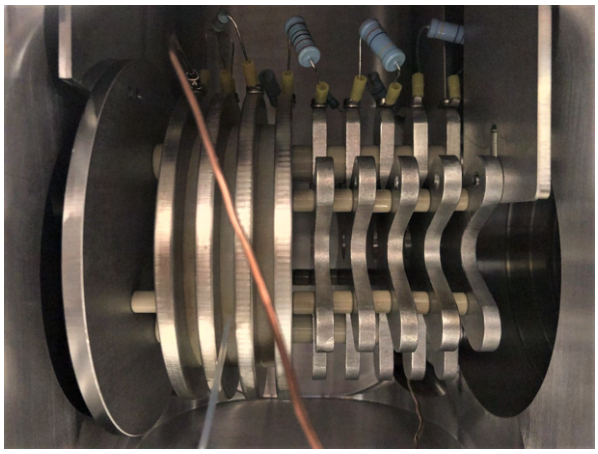

Figure 3.7: Electrostatic accelerator/gas cell unit placed in the beamline for the ISTF.

Throughout the experimental trials, it was found that when the incident H^- beam reached high beam power values certain components of the accelerator would surpass their operating temperature. This was found to be the case for resistors and insulators located in close proximity to the collimator. It was decided that water cooling would be implemented onto the collimator to dissipate most of the heat power which was causing these issues. A modified water cooled collimator was designed for the electrostatic accelerator assembly which was modeled using SolidWorks®. A thermal simulation was performed using SolidWorks® Simulation package to determine if the cooling provided would be sufficient to keep the temperature of the collimator and subsequent components under their respective maximum operating temperatures. Figure 3.8 displays the model of the modified collimator and thermal simulation results.

This simulation was performed with a heat load of 450 W distributed as a Gaussian distribution around the center of collimator. 450 W is the maximum beam power available from the H^- volume-cusp source. Copper was chosen as the material for the new water-cooled collimator as it would be easier to braze a cooling channel onto the face of the collimator and create a good thermal contact without needing to design an expensive collimator with an integrated cooling channel. Copper also has excellent thermal conductivity (413 W/(m K)) [54] creating effective heat transfer throughout the collimator to the cooling channel. As a result of the implemented cooling channel in the simulation, the maximum temperature of the collimator reaches a temperature of 71°C, this is below the maximum operating temperature of the resistors used for the design (155°C) [56] and the PTFE insulators used for the gas cell portion of the accelerator (260°C) [55]. In order to be able to fit the updated collimator with a cooling channel in the vacuum box, one of the electrodes had to be removed. Thus, the electric field profile had to be modified in order to maintain a quadratic electric field gradient. A new configuration was implemented with 8 electrodes (7 resistors) with the same gap size as the previous design. A diagram of the electrode configuration and resulting potential gradient of the shortened accelerator unit is shown in figure 3.9.

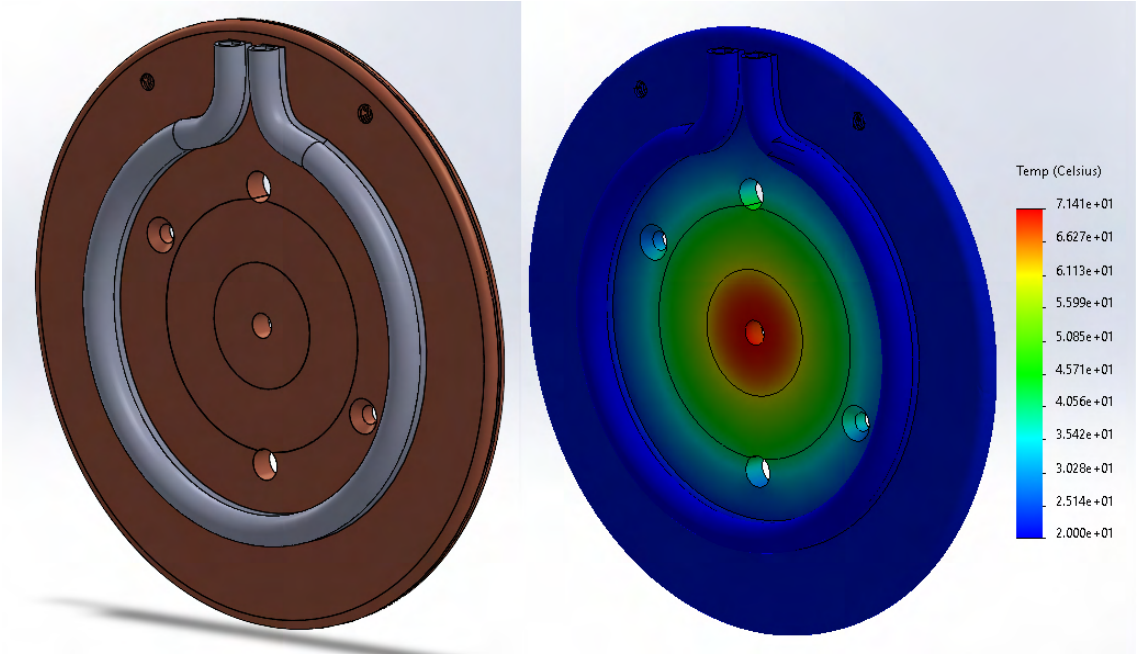

Figure 3.8: SolidWorks® model and thermal simulation of water cooled collimator with 450 W

The resistor values displayed in figure 3.9 are theoretical, akin to the values in table 3.2. Table 3.4 shows the values of the actual resistors used which were available for the configuration created with 8 electrodes.

Table 3.4: Actual resistor values used for the quadratic electric field gradient in the accelerator with 8 electrodes.

Resistor number	Resistance (MΩ)	Voltage drop (kV)
1	4.7	0.47
2	12	1.20
3	22	2.21
4	24	2.41
5	39	3.91
6	47	4.71
7	51	5.11

A copper tube was brazed onto the collimator plate and a water line connection was routed through the top plate of the vacuum box to supply a means of cooling while maintaining vacuum in the system. Figures 3.10 and 3.11 show the updated accelerator design with water cooling.

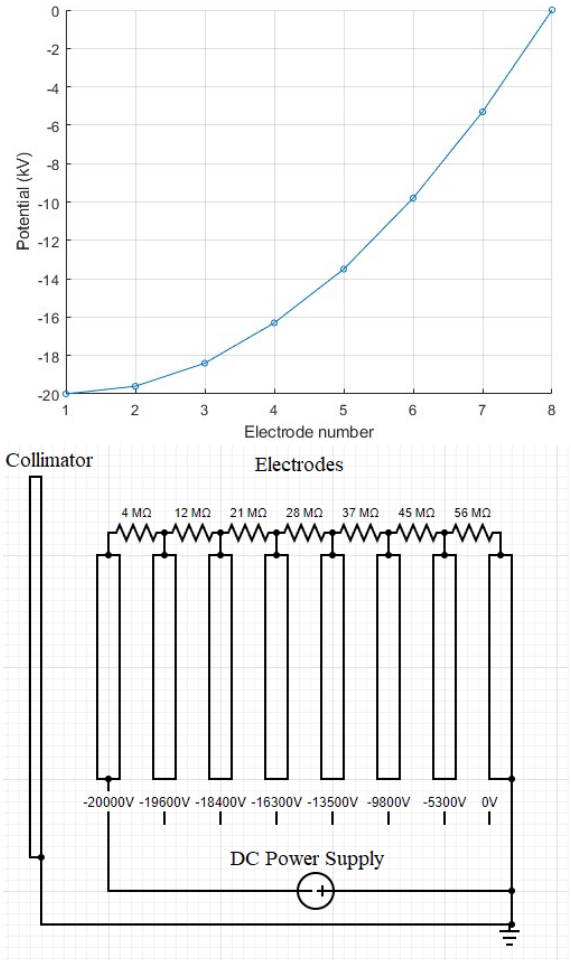

Figure 3.9: Plot of the potential values for each electrode in an updated 8 electrode accelerator design.

Before the updated electrostatic accelerator was implemented, a SIMION [57] electrostatic simulation was performed to ensure that the lenses still possessed a focusing effect. It was found that the focusing effect of the aperture lens system kept the beam from diverging and visual results of the simulation are shown in figures 3.12, 3.13, and 3.14. It should be noted that these simulations were performed by setting the associated potential values to the electrodes and collimator and flying 1000 H^- particles through the apertures at an energy of 30 keV.

It should be noted that for future experiments, a more extensive SIMION simulation should be performed to optimize the ion optics, especially when changing electrode configurations. A computational fluid dynamics software should be used in order to properly simulate different gas flows into the accelerator unit based and analyze the effects of different pressures of residual gas targets. That being said, the simulations show that the accelerator is not de-focusing at the ground electrode which is expected from a thin lens aperture approach, the beam enters a drift so the accelerator is overall focusing.

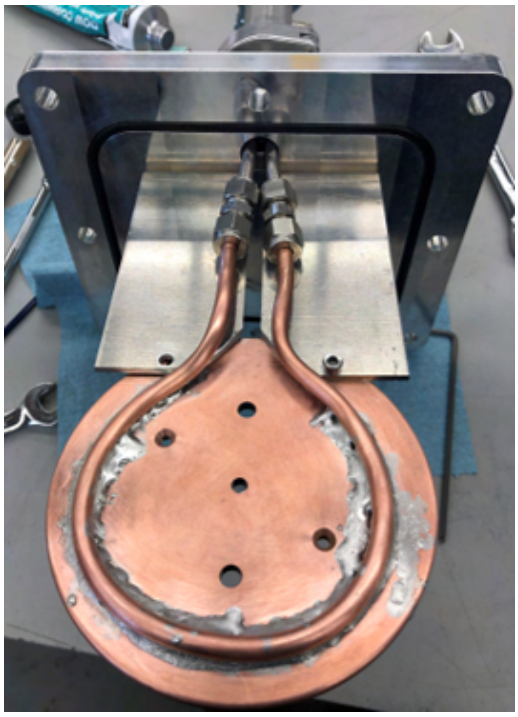

Figure 3.10: Cooling channel brazed onto the copper collimator.

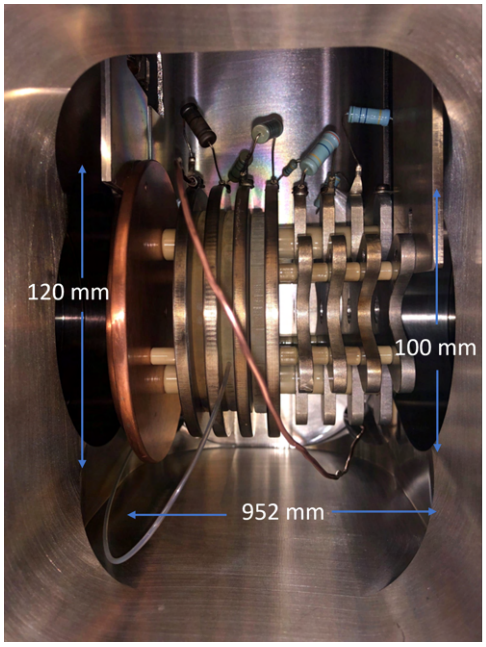

Figure 3.11: Electrostatic accelerator with a water cooled collimator in the beamline of the ISTF.

The water cooled collimator was found to keep components under their maximum operating temperature as fewer replacements of sensitive components were needed after operating at high beam power tunes.

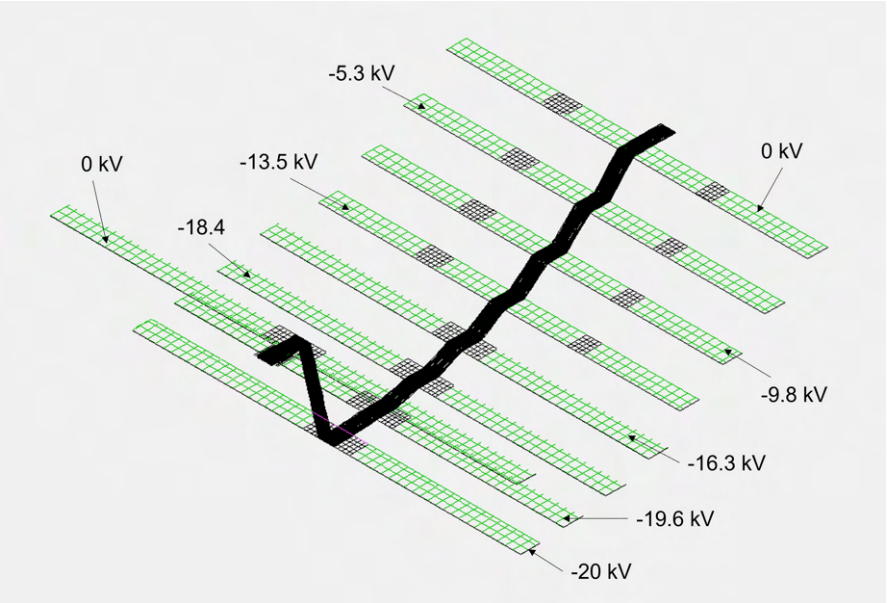

Figure 3.12: SIMION electrostatic simulation results for an 8 electrode accelerator unit showing potential profile of the electrostatic components.

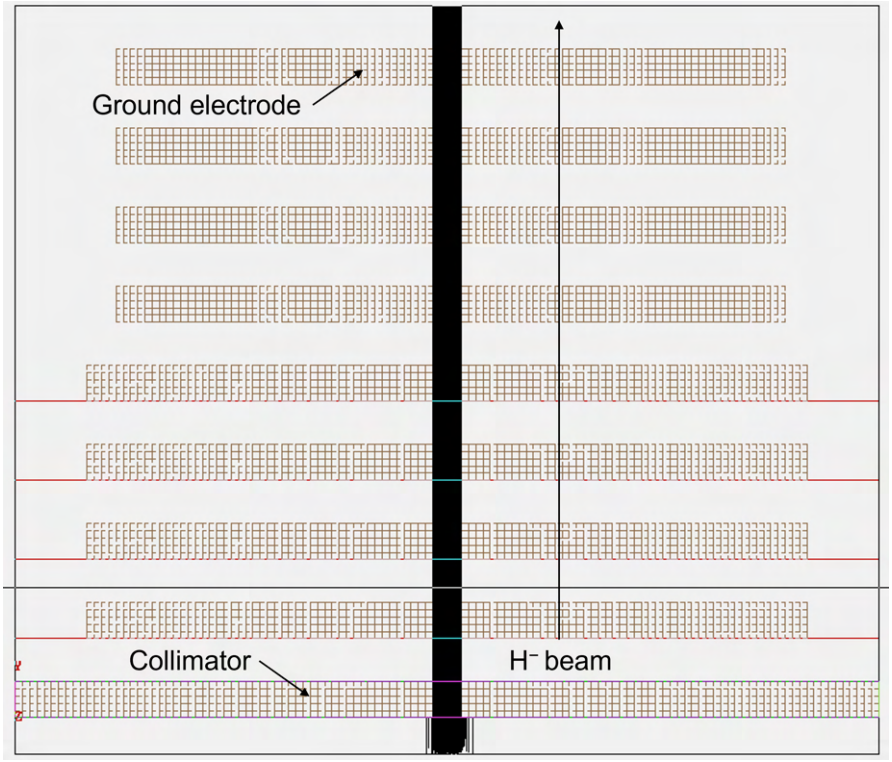

Figure 3.13: XY cross-section of SIMION electrostatic simulation with no residual gas injected.

Gas was injected into the accelerator unit using a voltage controlled mass flow controller [58] which was varied using a DAQ measurement hardware unit and allowed for a computer user interface to adjust the voltage applied to the mass flow controller. The potential applied to the accelerator unit was varied manually through the high voltage power supply unit.

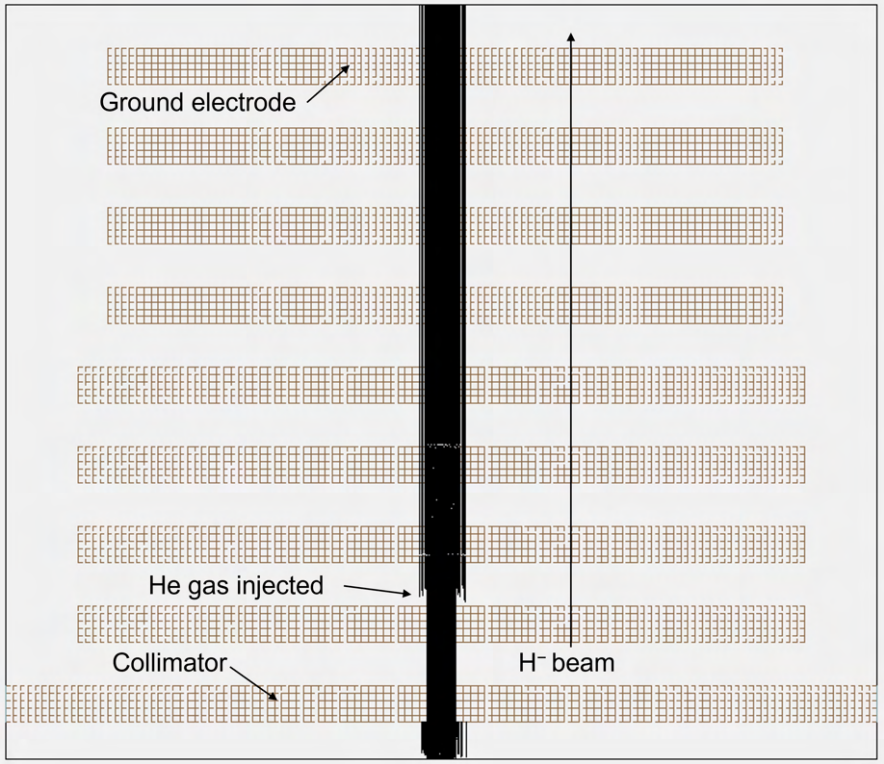

Figure 3.14: XY cross-section of SIMION electrostatic simulation with 1000 particles of helium injected at 20 eV kinetic energy.

In order to measure the current after the collimator of the electrostatic accelerator, a small fixed Faraday cup was needed which was not readily available. Thus, a Faraday cup was designed, constructed and assembled for this project. The development is described in sub-section 3.4.

3.4 Custom Faraday cup design

A stationary custom Faraday cup was design and constructed for the purpose of measuring the ion beam current at different locations which could not be obtained by the two Faraday cups already in the beamline of the ISTF. The Faraday cup was designed so that it could easily be attached to the downstream side of the collimator and ground electrode of the electrostatic accelerator described in section 3.3. The Faraday cup is intended to stop the ion beam which has passed through the collimator and accelerator unit and measure the total current by suppressing any secondary electrons which could be emitted through collisions with the ion beam and the Faraday cup material. A simple diagram of the Faraday cup design is shown in figure 3.15, where the Faraday cup is isolated from ground through ceramic standoffs, has a measurement lead which allows for current to be recorded, and includes permanent magnets for secondary electron suppression.

The material chosen for the Faraday cup was selected based on the electrical conductivity, secondary electron emissions, maximum operating temperature, cost and availability. Graphite is known to have sufficient electrical conductivity for Faraday cup applications and has excellent properties for reducing secondary electron emissions [61], [62],

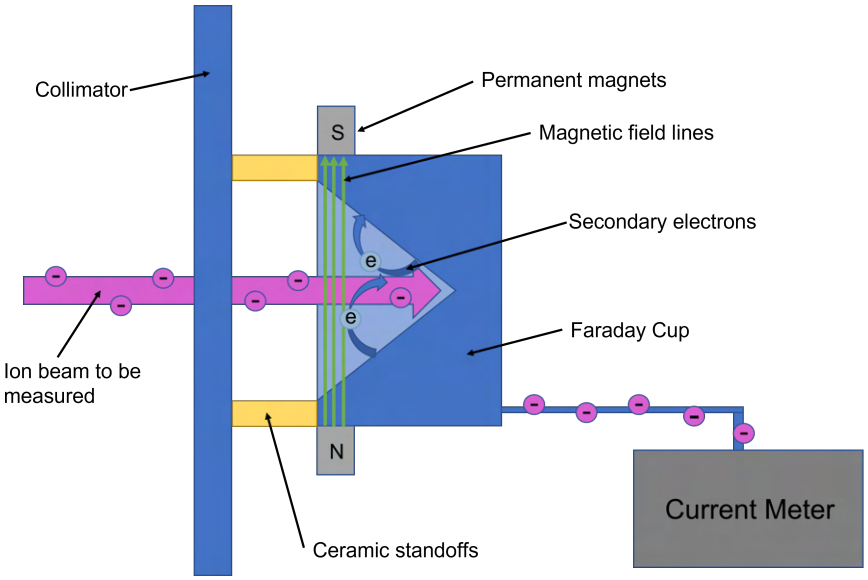

Figure 3.15: Diagram of custom Faraday cup design mounted to the downstream end of the collimator.

[63]. Graphite also has a high maximum operating temperature of 427°C [64] and is a readily available material that can be machined using a CNC system. The Faraday cup was designed using SolidWorks® [65] and a magnetic simulation was performed using FEMM [66] to ensure that the magnetic field strength of the permanent magnets being used was sufficient for recapturing all secondary electrons. Secondary electrons emitted from a material are caused by the excitation of electrons within the target material from incident electrons (or ions) which cause a chain reaction from atom to atom which can eventually result in the emission of electrons on the surface of the material. The electrons which are excited always have an energy lower than the electron which excites them, thus the maximum energy of secondary electrons is found to be 50 eV [67]. The results from the FEMM simulation are shown in figure 3.16.

As seen in figure 3.16, the minimum magnetic field strength is 0.05 T in the region of interest where the incident beam is impinged. To ensure that all secondary electrons were captured within the Faraday cup a calculation of the bending radius of electrons with a kinetic energy of 50 eV through a 0.05 T field was determined. The target bending radius should be less than half of the length of the smallest lip on the Faraday cup which is 2.5 mm i.e. $\leq$ 1.25 mm. The momentum value of 50 eV electrons was calculated to be 7149 eV/c by equation 2.12, thus the bending radius ρ for a field strength B of 0.05 T was found to be 0.48 mm by equation 2.18. SmCo17 magnets were chosen for the permanent magnets as they have a high operating temperature of 300°C [68] and supply the same magnetic field strength as the permanent magnets in the simulation shown in figure 3.16. Figure 3.17 displays the machined and assembled custom Faraday cup. A connection lead was attached to the back of the Faraday cup and connected to a BNC port which allowed for electrical signals to be transferred out of the vacuum box while maintaining the required pressures.

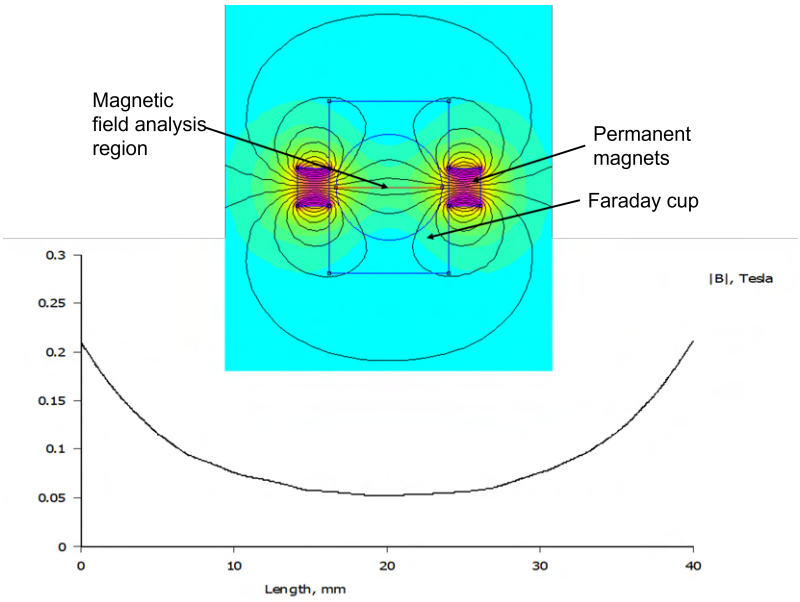

Figure 3.16: FEMM magnetic simulation for custom fixed Faraday cup

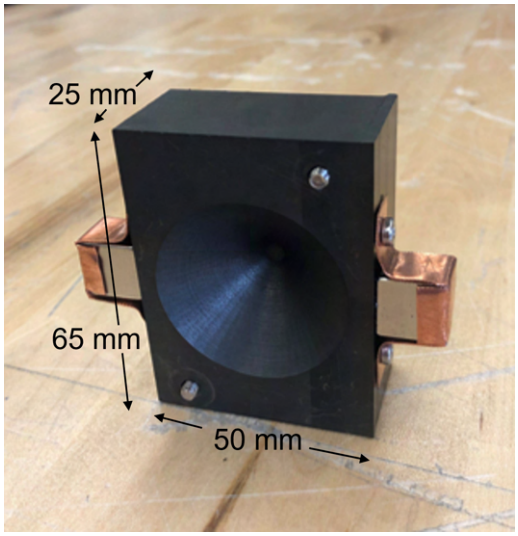

Figure 3.17: Custom Faraday cup for measuring beam current before and after electrostatic accelerator unit with dimensions.

The experimental test setup utilized some features which are standard products of D-Pace. The following two sub-sections give a brief explanation of the mass spectrometer system and 600 W fixed Faraday cup respectively.

3.5 Mass spectrometer

The mass spectrometer system used for this project was a 1:500 resolution mass spectrometer. The resolution of the spectrometer is defined as an energy resolution, meaning that for a given energy E_0 an energy of $(1+1/500)E_0$ can be distinctly differentiated. It should be noted that the acceptance slits on the upstream and downstream sections of the magnet have a great effect on the resolution. Minimizing the slit width creates a more resolved beam. The magnetic rigidity $B\rho$ of the mass spectrometer, as defined in equation

2.18, is 0.2196 T·m with a bending radius of 191 mm, a bending angle of 90°and a maximum magnetic field strength of 1.15 T. More information on the technical specifications of the mass spectrometer dipole magnet can be found at [48]. Figure 3.18 displays an image of the mass spectrometer system used for all experiments performed.

Figure 3.18: 1:500 resolution mass spectrometer dipole magnet in the beamline of the ISTF.

In order to adjust the current applied to the mass spectrometer from a computer interface a program was developed using LabVIEW [59]. LabVIEW is a graphical programming software that is typically used for automation purposes, in this case a program was developed to communicate with the current power supply for the magnet so that the magnetic field strength could be easily varied. The program was originally designed to sweep a current range on the mass spectrometer and simultaneously collect the associated beam current data measured on the fixed Faraday cup downstream of the mass spectrometer dipole. This data was automatically exported to a .csv file that could used for data analysis. The program was modified to allow for the magnet current to be set to a fixed value in order to closely analyze detection regions on the mass spectrometer current range. Figure 3.19 displays the user interface and graphical program which was created for current control of the dipole magnet.

3.6 Fixed Faraday cup and picoammeter

A 600 W water-cooled fixed Faraday cup was used to collect the separated ion beams after the mass spectrometer dipole which is an existing product of D-Pace [48]. The Faraday cup includes an adjustable acceptance slit (0-20 mm acceptance) and electrostatic suppression for secondary electron emission. This electrostatic suppression was found to create a significant amount of noise in small current detection signals, thus, it was replaced by a set of SmCo17 permanent magnets which improved the sensitivity of the detector. Larger current beams that were not effected by the noise produced by the electrostatic suppressor were measured with both permanent magnet and electrostatic secondary electron suppression and were found to have no detectable difference on current values recorded. The current was read through a 6485 Keithley picoammeter [60] which was able to display a 0.1 nA resolution after noise reduction from nearby electrical signals and built-in

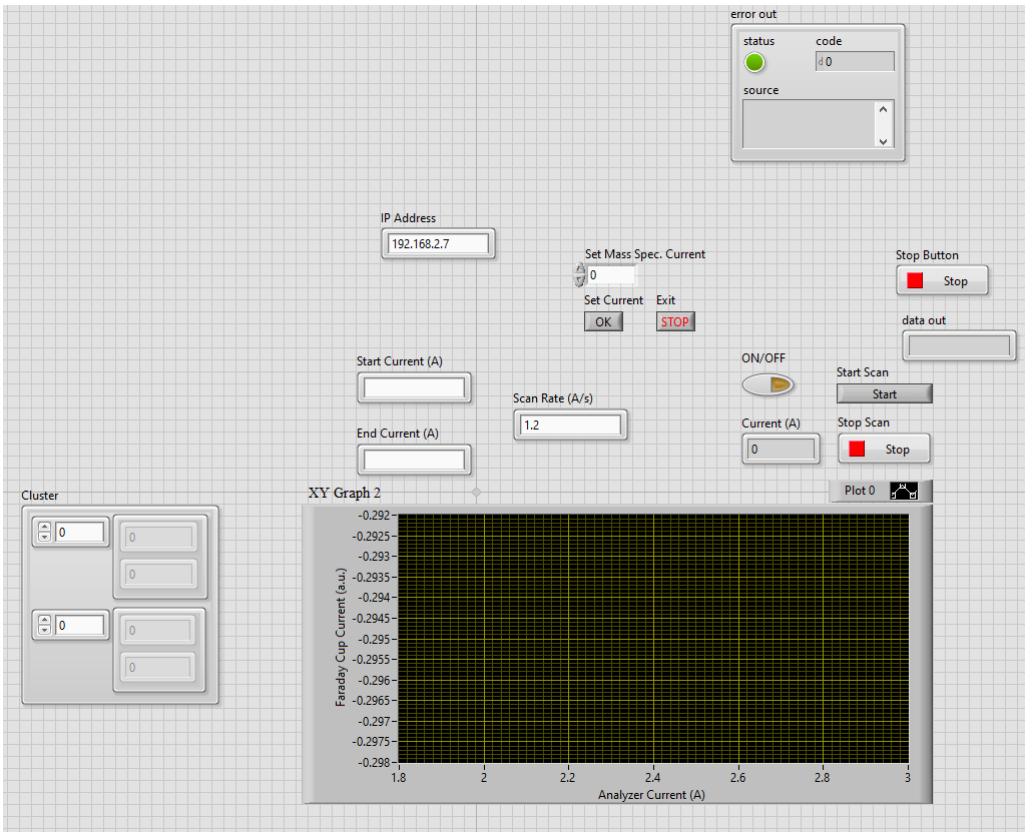

Figure 3.19: User interface of LabVIEW program created for mass spectrometer magnet control

filtering techniques available through the picoammeter. The mass spectrometer was calibrated using the primary incident H^- beam at varying energies. The momentum of these beams was known and the mass spectrometer currents at which they were detected was used to characterize the mass spectrometer by equation 2.25.

As well as measuring parameters such as beam current, it was important to record the pressure of the beamline. The next sub-section will describe the vacuum system of the beamline and vacuum simulation used for further pressure analysis.

3.7 Vacuum system and Molflow+ simulation

The ISTF is fitted with three wide range combination vacuum gauges [69]. The gauges are mounted in different positions which are labeled in figures 3.20, 3.21, and 3.22. These vacuum gauges are suited to read pressures between atmosphere and 10^{-9} mbar and use Pirani and inverted magnetron technology [70] [71]. The vacuum system on the ISTF is equipped with three turbomolecular vacuum pumps [72] [73] which are also shown in figures 3.20, 3.21, and 3.22. In order to measure a cross-section for the H^- beam incident on the neutral gases, the pressure within the charge exchange cell where the collision takes place must be known. Due to the placement of the electrostatic accelerator and the location of available ports to connect the vacuum gauges, the pressure at the point of collision could not be directly measured. Thus, a model was created using Molflow+ 2.8.6 [74] to simulate the pressures in the vacuum system where a gauge cannot reach for an

accurate reading. Molflow uses the test particle Monte Carlo method in order to calculate the pressure profile of the geometry being analyzed [75]. The amount of test particles is scaled up to simulate real pressure values and the particles are tracked until they are pumped out of the system.

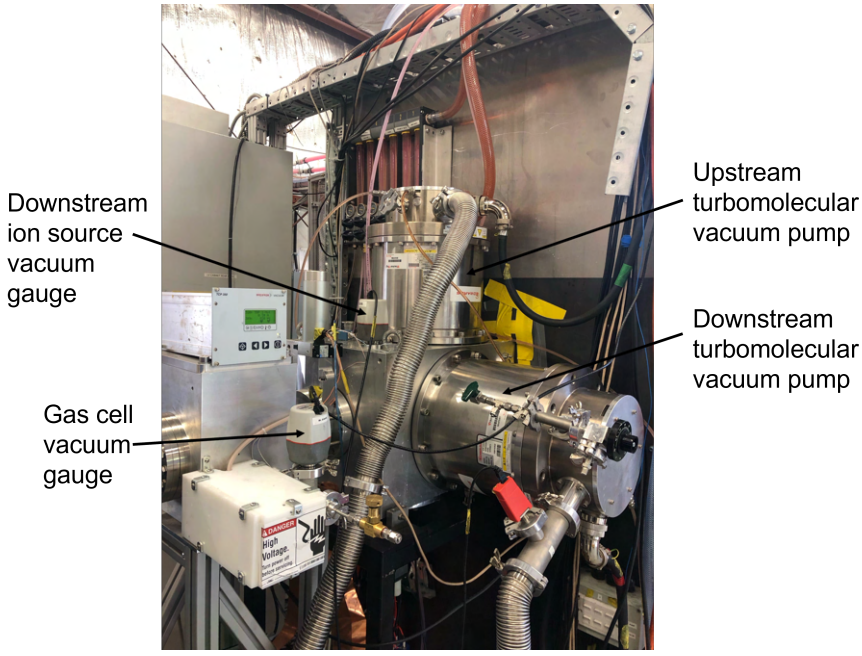

Figure 3.20: Ion source and gas cell portion of the ISTF with vacuum pumps and gauges labeled.

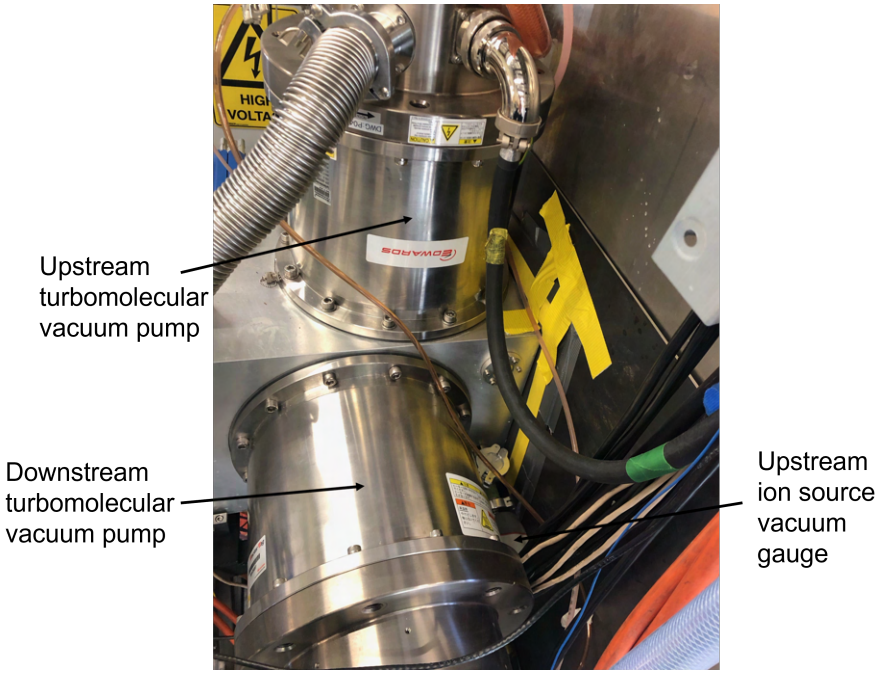

Figure 3.21: Ion source portion of the ISTF with vacuum pumps and gauges labeled.

The ion source vacuum box and charge exchange vacuum box were imported into Molflow from SolidWorks® files while the volumes for the remainder of the beamline

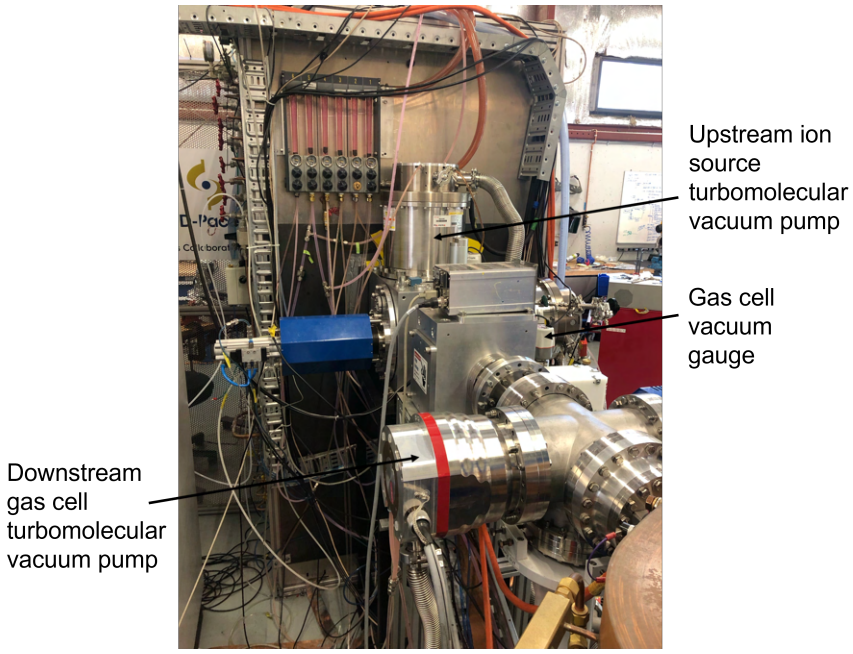

Figure 3.22: Gas cell and downstream beamline of the ISTF with vacuum pumps and gauges labeled.

were assembled within the program. All outgassing rates of every surface were set to a minimum value for clean baked vacuum surfaces of 4×10^{-13} Torr·L·s^{-1}·cm^{-2} [76] and all pumping faces were set to their specified pumping speeds, 1700 L/s and 555 L/s for H_2 respectively [72] [73]. Pressure plotting points were added in the regions in which the pressure gauges are located in order to compare the pressure in the simulation with the pressure in the actual system measured at the same point. From this point, all outgassing rates of the vacuum faces were incrementally increased until a base pressure was reached that was comparable to the lowest pressure read on any of the gauges when no gases were injected into the system. The vacuum gauges were located in different positions throughout the ISTF and would read different values as a result of the pumping capabilities in those regions and the outgassing of materials close by. Suspected high outgassing surfaces had their outgassing rates increased in the model until all pressure plots representing each gauge read the same value as the actual gauges under the same conditions. This gives an approximate model of the pressure throughout the vacuum system of the ISTF without having vacuum gauges located in difficult placement areas. It is very important to state that Molflow is meant to model vacuum systems in the high and ultra high vacuum regimes. The pressure being simulated in the gas cell is likely outside of this acceptable regime in which Molflow can accurately model the pressures. With this being said, the following simulations shown should be taken as a guideline for the pressure and are likely susceptible to significant error.

An image of the modeled vacuum system is shown in figure 3.23 with key elements labeled.

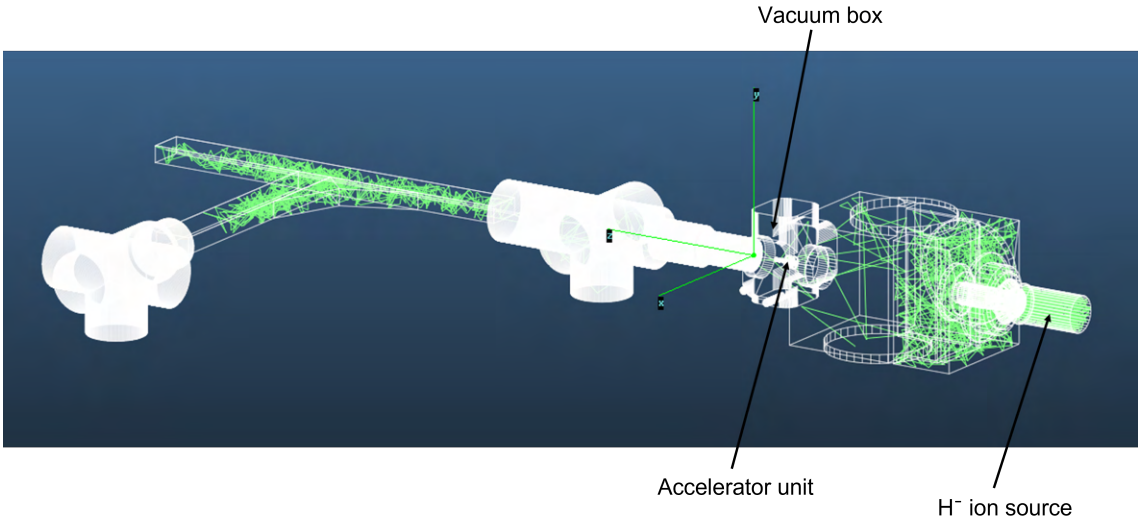

Figure 3.23: Molflow model of ISTF vacuum system simulation.

Figures 3.24 and 3.25 show a pressure profile of the vacuum system in the beamline plane as it approaches the mass spectrometer dipole. It should be noted that the vacuum gauge which was used to characterize the pressure off the vacuum box containing the electrostatic accelerator was located on a cross down a narrow diameter vacuum pipe. The poor conductance of this system leading to the gauge, coupled with high pressures attempting to be simulated likely resulted in an improper characterization of the pressure in this region. When initially characterizing the pressure in the system, the high pressure measured in the gas cell region was attributed to the outgassing of materials used for the electrostatic accelerator. Over time, it was determined that the poor conductance of the vacuum pipes connecting the gauge was the likely cause. In the future a gauge would be placed closer to the position in which the electrostatic accelerator is located, although, this does not solve the incompatibility with high pressures that Molflow faces.

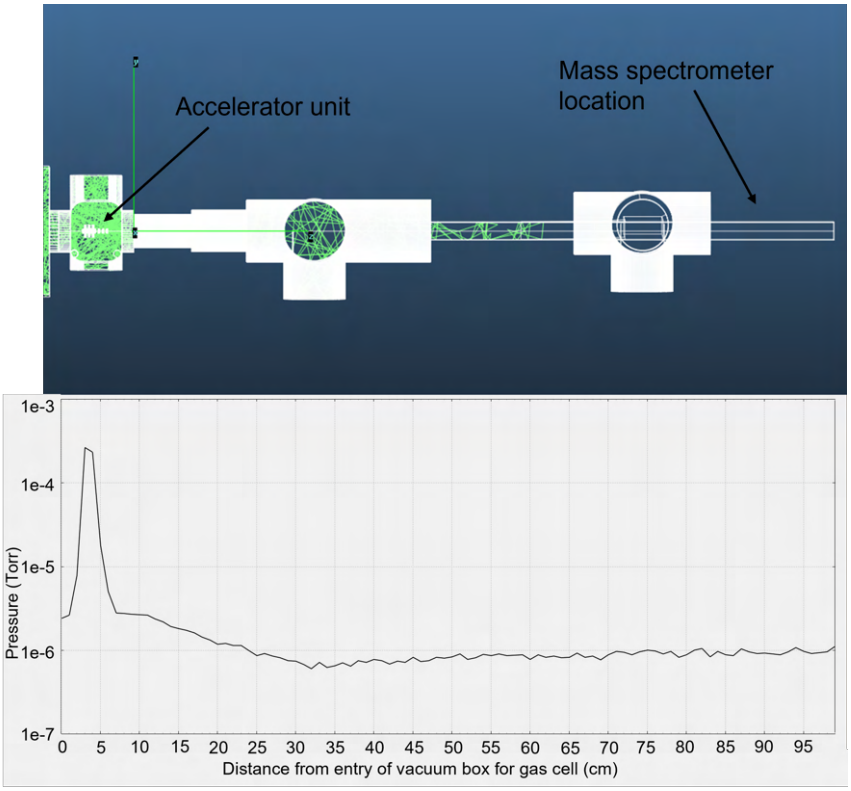

Figure 3.24: Pressure profile of the Molflow simulation with no gas injected into the electrostatic accelerator.

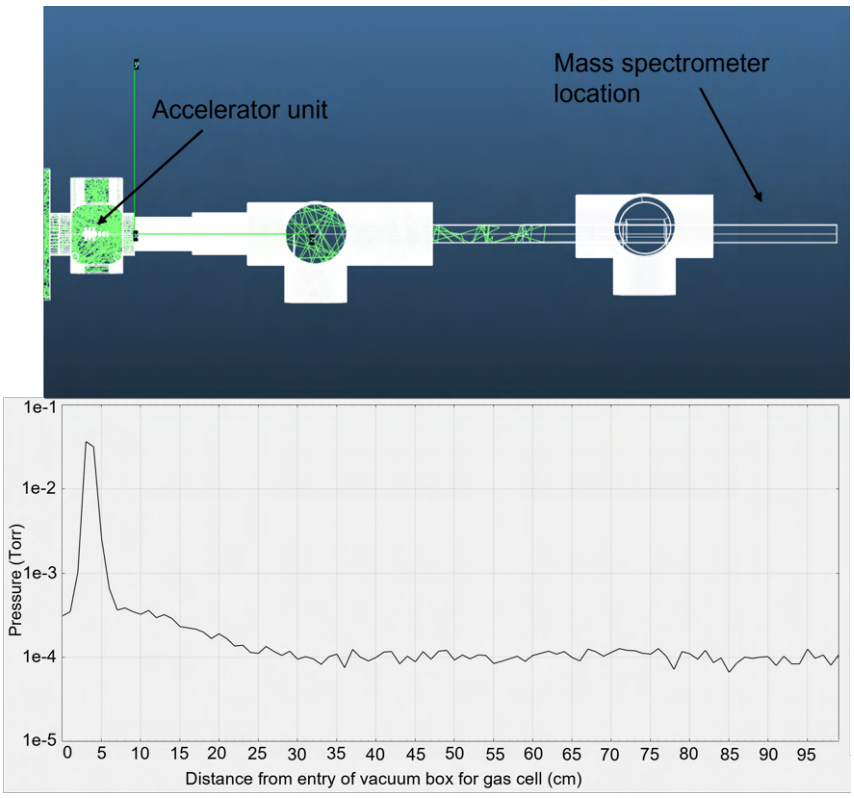

Figure 3.25: Pressure profile of the Molflow simulation with 6 sccm of helium injected into the electrostatic accelerator.

Chapter 4

Producing negative ions using an H^- ion source

4.1 Impinging H^- beam on neutral gases

The D-Pace TRIUMF licensed volume-cusp ion source is capable of producing relatively well-focused H^- beams at energies ranging from 15-30 keV with beam currents from 0-15 mA. These parameters were swept so that the incident beam characteristics for optimal negative ion conversion rates could be found. It was also important to understand the amount of incident H^- beam entering and exiting the gas cell accelerator unit since this is required for obtaining a conversion rate of He^-/H^- for negative helium ions produced. The custom stationary Faraday cup that was described in section 3.4 was mounted to the downstream side of the collimator at distance equal to the spacing between the collimator and the first electrode. The current transmission through the collimator was calculated by measuring the voltage drop across a 4.7 kΩ load resistor which was connected from the Faraday cup to the ground reference of a digital volt meter with a precision of 0.1 mV. A diagram of this particular experimental setup is displayed in figure 3.15. The following tables show the current transmission for 20 keV and 30 keV beams given a range of incident beam current values.

Table 4.1: Transmission of a range of beam current values for a 20 keV H^- beam incident on the copper collimator with 5 mm aperture recorded with a custom fixed Faraday cup.

Incident beam current (mA)	**Beam current after collimator (μA)**
0	0
-1.01	-33.0
-2.98	-121.5
-4.99	-276.6
-7.00	-336.2

It should be noted that the current range for the 20 keV and 30 keV data sets is different due to the difficulty of producing a relatively well-focused 20 keV beam at higher beam current values. This is likely due to a combination of the extraction electrodes being fixed at a distance that is optimized for a 30 keV beam, and effects of space charge due to lowering the beam energy. It should also be noted that the full current range of 0-15 mA was not tested as it was found that damage would occur to the accelerator unit at full beam

Table 4.2: Transmission of a range of beam current values for a 30 keV H^- beam incident on a copper collimator with 5 mm aperture recorded with a custom fixed Faraday cup.

Incident beam current (mA)	Beam current after collimator (μA)
0	0
-1.01	-36.6
-3.03	-119.2
-5.00	-246.6
-6.99	-376.2
-9.06	-553.6
-11.01	-734.7

power for longer test periods despite the collimator cooling efforts. A linear regression of the data was performed to give a formula for current transmitted through the collimator at the entrance of the accelerator unit. Figures 4.1 and 4.2 show the plotted values with the linear trendline formula displayed. It should be noted that the error associated with the beam current measurements in these plots is the reading error of the measurement equipment used, 0.05 μA and 0.05 mA for the y-axis and x-axis respectively. This error is not visible on this scale with error bars.

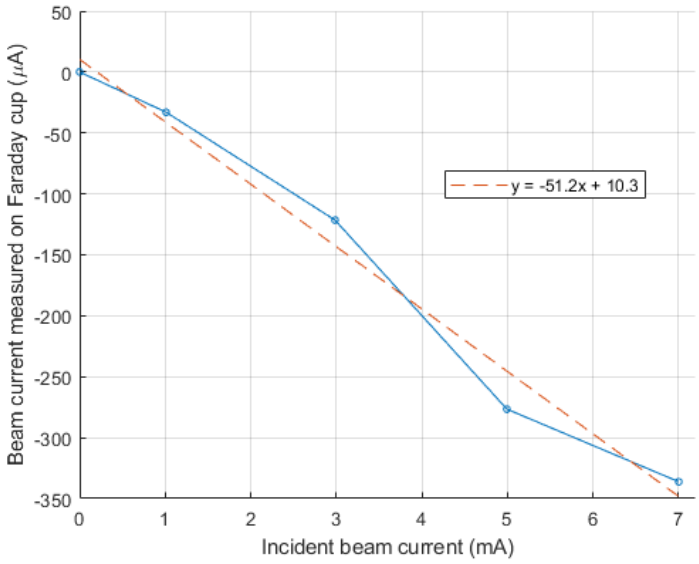

Figure 4.1: Plot of results from table 4.1 with a linear regression of the data and the resulting linear formula displayed.

In terms of cross-section, the total electron loss cross-section of H^- on He in the gas cell was calculated before the experiment to determine if the charge exchange could be significant enough to produce beams of He^-. The incident H^- beam was measured before and after the charge exchange cell unit with varying flow to calculate the total electron loss cross-section by equation 2.30. Table 4.3 shows the measured beam current before I (downstream of the collimator) and after I_0 (downstream of the final electrode) the accelerator unit using the custom Faraday cup and the measurement technique described above. A 30 keV H^- beam at 2.7 mA was impinged on the accelerator unit with He gas flow varying from 0 sccm to 6 sccm.

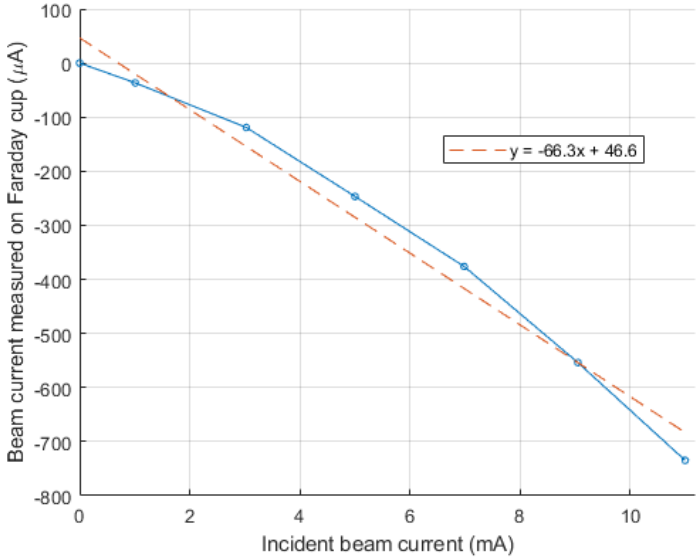

Figure 4.2: Plot of results from table 4.2 with a linear regression of the data and the resulting linear formula displayed.

Table 4.3: Beam current transmission measurements through the gas cell accelerator unit with varying helium flow for a 30 keV H^- beam incident on the collimator at 2.7 mA.

He gas flow (sccm)	**Pressure inside gas cell from Molflow (Pa)**	I **(μA)**	I_0 **(μA)**
0	2.04 x 10^{-4}	-116.2	-112.2
2	1.08 x 10^{-2}	-116.2	-100.7
4	2.18 x 10^{-2}	-116.2	-90.1
6	3.29 x 10^{-2}	-116.2	-77.1

From table 4.3 $\ln(I/I_0)$ can be determined for each associated pressure value and a linear plot can be produced. Said plot is shown in figure 4.3 with the equation of the trendline displayed outlining the slope of the line. The error associated with this plot is not quantifiable as the approximation of pressure using Molflow has an immeasurable inaccuracy due to the lack of precision high pressure capabilities of the software.

The slope of this line is determined to be -12.45 (Pa^{-1}), thus with a known charge exchange cell length and temperature, the total electron cross-section can be calculated by equation 2.33. That being said, the exact length of the gas cell which occupies the specified pressure is not well defined from the Molflow simulation especially because Molflow does not produce accurate results at high pressure regimes. In order to get a more accurate cross-section measurement the region in which the gas target is defined and the exact pressure of that region must be very well known. Also, the temperature at the location in which the collision occurs cannot be accurately measured so a range of cross-section values is calculated based on the extreme limits of these two unknowns.

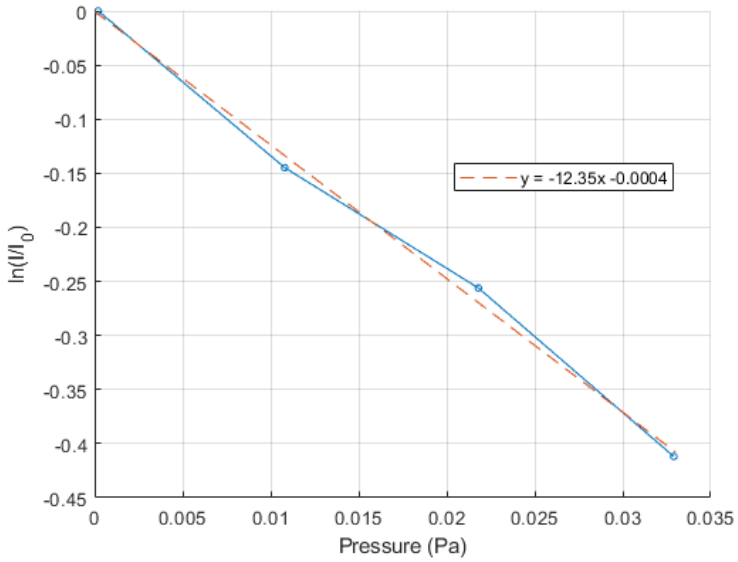

Figure 4.3: Natural logarithm of the beam current transmission ratio of a 30 keV H^- beam through the gas cell versus the relative pressure inside the gas cell.

The length of the gas cell x is projected to be between 9.35 cm and 3.26 cm, where 9.35 cm is the full length of all the electrodes and 3.26 cm is the length of the semi-contained region in which the gas is injected. The temperature range is spanned between 20-70 °C (293-343 K) based on the ambient room temperature and the maximum temperature of the collimator with full beam power as outlined in figure 3.8. To get a range of cross-section values, one calculation is performed with a charge exchange cell length of 9.35 cm and 293 K, while the other is carried out with a length of 3.26 cm and a temperature of 343 K. The resulting total electron loss cross-section range for this experimental setup for an H^- beam incident at 30 keV is 5.34 x 10^{-15} cm^2 to 1.79 x 10^{-14} cm^2. Although this range gives the possibility for the total electron cross-section to include a charge transfer cross-section component which could lead to the production of He^- beams, it should be emphasized that this is a very crude approximation with an error which could place the cross-section outside of the acceptable range for effective charge transfer.

4.1.1 H^- on He

The original concept for this project was based around the production of He^- using neutral helium gas and the charge exchange method outlined by Doupé and Litherland. Helium was chosen as the original target gas as it is known to have useful industrial applications in the ion implantation industry [8] which experiences contamination issues resulting in defective silicon chips with the present production method of using alkali vapours for charge exchange [12], [77]. Injecting helium directly into the D-Pace TRIUMF licensed ion source was previously performed with hopes of extracting negative helium ions, the results found that no detectable amount of He^- were extracted from the source [78]. The charge exchange cell/electrostatic accelerator that was developed for this project and is described in section 3.3 was used in an attempt to create and measure negative helium ions. Neutral helium gas was injected into the constructed accelerator unit with an H^- beam passed through the gas target region at an energy of tens of keV. The potential applied to the accelerator unit was used to accelerate any newly formed negative helium ions

that were to be measured on the fixed Faraday cup downstream of the mass spectrometer system. The conversion in equation 4.1 was the goal of this experiment.

$$H^- + He \rightarrow H + He^- \tag{4.1}$$

The electron affinity of of the two species (H = 0.75 eV, He = 0.08 eV) [79] [13] is within 1 eV, allowing for a potential near-resonant charge transfer. Although, the electronic transfer to He^- may forbidden if the target helium is in the ground state $(1s^2)^1S$ and not the excited triplet state $(1s2s)^3S$. This information was better understood once experiments using helium as a target had already been performed. The industrial significance of He^- and absence of any known previous experiments exploring this type of collision gave enough motivation to test neutral helium gas as a target for negative ion production. For the experimental process, the gas flow was adjusted between 2-6 sccm which was found to create acceptable pressures within the accelerator unit so that electrical breakdowns were not frequent with tens of kV applied to the accelerator due to Paschen's law [50]. The potential of the accelerator was adjusted up to 18 kV and the incident beam of H^- was directed the gas cell unit with energies ranging from 15-30 keV and beam currents up to -12 mA, approximately -750 μA after the collimator which is based on the results from figure 4.2. The current applied to the dipole magnet of the mass spectrometer system which would allow for He^- detection was derived in section 2.5 and displayed as equation 2.25. Given that the mass, charge, and energy of both the incident H^- beam and the potential resulting He^- beam are known, the upper limit of current detection (I_{He^-}) can be found. Table 4.4 displays the mass spectrometer current at which He^- would be detected for different accelerator potential values (E_{He^-}) given that a 30 keV (E_{H^-}) beam of H^- is detected at 8.3 A (I_{H^-}) on the mass spectrometer dipole. Note that the mass of H^- and He^- was taken to be 939 MeV/c^2 and 3724.5 MeV/c^2 respectively.

Table 4.4: Theoretical He^- beam energy versus mass spectrometer current for detection.

Accelerator Potential E_{He^-} (kV)	**Mass Spec. Current I_{He^-} (A)**
20	13.50
18	12.80
16	12.07
14	11.29
12	10.45
10	9.54
8	8.54
6	7.39
4	6.04
2	4.27

No He^- was detected at a resolution of 0.1 nA for any combination of incident beam parameters and gas cell accelerator settings. A table listing all of the experimental parameter combinations and the resulting beam current measurements when using helium as a target can be found in table 4.5.

Figure 4.4 shows a plot of the results from a test with a 30 keV incident H^- beam with 18 kV applied to the accelerator unit and 6 sccm of neutral He flow into the gas cell

Table 4.5: Variable experimental parameters for tests with a helium target and the corresponding beam current intensities associated with each combination of test settings.

		Incident beam energy (keV)			
		15	20	25	30
		Incident H^- beam current (mA)			
		1-6	1-7	1-10	1-11
		Gas flow (sccm)			
		0-8	0-8	0-8	0-8
		Intensity of peak measurement $\pm$ 0.1 (nA)			
Accelerator Potential (kV)	2	0.1<	0.1<	0.1<	0.1<
	4	0.1<	0.1<	0.1<	0.1<
	6	0.1<	0.1<	0.1<	0.1<
	8	0.1<	0.1<	0.1<	0.1<
	10	0.1<	0.1<	0.1<	0.1<
	12	0.1<	0.1<	0.1<	0.1<
	14	0.1<	0.1<	0.1<	0.1<
	16	0.1<	0.1<	0.1<	0.1<
	18	0.1<	0.1<	0.1<	0.1<
	20	0.1<	0.1<	0.1<	0.1<

portion of the accelerator. It should be noted that the expected mass spectrometer current region for secondary negative ion detection is any current value up to the values calculated by equation 2.25. In theory, the negative ion could be created at any point in the accelerator unit where a collision occurs, thus, if it is not created at the first electrode of the accelerator it will not see the full potential. This would result in a lower energy beam which would be detected at a lower mass spectrometer current value.

The region for negative helium ion detection was limited due to the similarity in mass between the incident beam (H^-) and the target gas (He) since the varying energies can create a significant overlap in the detection region in which the primary incident beam (H^-) will overpower any possible negative helium signal. This resolution between the beams could be greatly improved for future experiment through optimization of the beam optics. Another limiting factor for secondary negative ion beam detection is the measurement of tens to hundreds of nA of positive beam current at mass spectrometer currents up to 2.5 A higher than the area of incident H^- beam measurement as shown in figure 4.4. The positive beam current measured in this region does not yield consistent values within 2-5 nA making it difficult to filter out as a background benchmark. The potential of the accelerator was also limited by voltage breakdown events when higher potentials were applied to the accelerator unit, likely due to a low point on the Paschen curve within the gas cell.

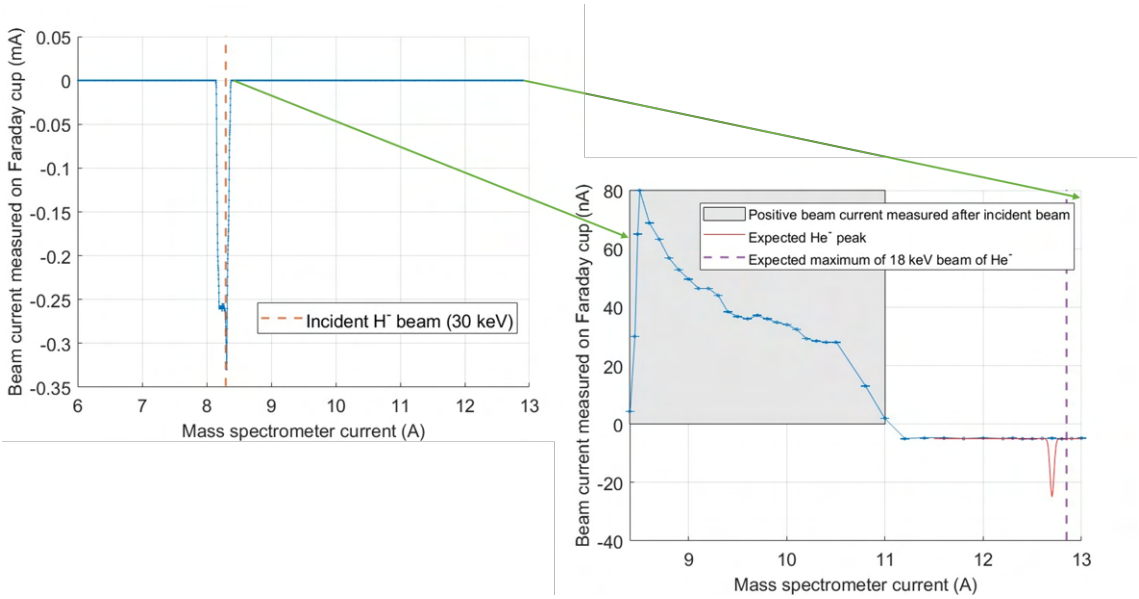

Figure 4.4: Current measured on Faraday cup as a function of mass spectrometer current for 30 keV, 3.5 mA H^- beam incident on 6 sccm of He flow injected into the gas cell. A dotted line shows an example of what a 20 nA signal of a He^- beam at 18 keV would look like. From equation 2.25, it is expected that the maximum mass spectrometer current that an 18 keV He^- beam can be measured is 12.86 A.

Outside of the restricted detection regions the measurement of He^- was likely not observed at a resolution of 0.1 nA due to the target helium being in the ground state of $(1s^2)^1$ which doesn't allow for a transition to the only known metastable He^- state $(1s2s2p)^4$. The metastable negative helium ion state $(1s2s2p)^4$ has three known angular momentum configurations, $J = 1/2$, $J = 3/2$, $J = 5/2$, all of which have a different lifetime. One of the most recent measurements of the lifetime of these He^- states before auto-electron detachment takes place was performed by Reinhed et. al. and the weighted average of the results are as follows: $J = 1/2 : 7.8 \pm 1.0 \mu s$, $J = 3/2 : 12.3 \pm 0.5 \mu s$, $J = 5/2 : 359 \pm 0.7 \mu s$ [80]. A possible reason for the lack of negative beam current detection from He^- could be that auto-detachment occurs before the beam is collected in the Faraday cup. Although, after a quick non-relativistic velocity calculation it is determined that this is an unlikely limitation of the experiment seeing as a 2 keV He^- beam would travel approximately 2.5 m in the shortest lifetime of an He^- ion (7.8 μs) which is almost 1 m longer than the distance between the accelerator unit and the fixed Faraday cup (1.6 m).

After it was confirmed that beams of He^- were not detectable using this experimental setup with a 0.1 nA resolution, the other neutral gas targets were considered for testing. This project was intended to investigate negative ion formation and charge exchange without the use of metallic vapours. Although negative helium ions have a known commercial application in the semiconductor industry, the other chosen gas targets could provide insight into the formation of negative ions using this novel technique for negative ion formation. Without making major modifications to the apparatus and experimental procedure given the limited time frame of this project, different neutral gases (X) would be considered to inject into the gas cell in order to explore the creation of different negative ions using the same technique as described in this section. The general charge exchange which is to be studied in this extension of the project is outlined in equation 4.2.

$$H^- + X \rightarrow H + X^- \tag{4.2}$$

The neutral gases chosen for this extension of this project were primarily picked based on the prospect of negative ion production from the target gases. Each gas selected has formed negative ions through ionization methods different from the charge exchange process of 4.2. This indicates that the negative ions are physically feasible but an opportunity is created for discovery science measurements which could have industrial or research applications unknown to the scientific community at this time.

4.1.2 H^- on H_2

H_2 was selected as a target gas as it was readily available by using the same supply that is used for the D-Pace TRIUMF licensed ion source which is used as the H^- driver. The objective was to create a secondary beam of H^- at an energy differing from the primary incident H^- beam as a proof of concept experiment. The electron affinity of H_2 is not well defined, but a measurement taken by McWeeny gives a value approximated to 2 eV [81]. This would be off-resonant for an interaction with a hydrogen ion beam likely resulting in a small charge transfer cross-section, but the availability of this target gas allowed for reasonably quick experimental setup and it was to be tested anyway. The exchange to H_2^- was also explored and equations 4.3 and 4.4 outline all possible charge transfer reactions for a beam of H^- incident on neutral H_2 gas.

$$H^- + H_2 \rightarrow H + H_2^- \tag{4.3}$$

$$H^- + H_2 \rightarrow H + H_2^{-*} \rightarrow 2H + H^- \tag{4.4}$$

The expectation of the charge transfer outlined in equation 4.4 was that the incident H^- beam would transfer an electron to the H_2 gas to form a metastable H_2^{-*} ion which would decay into an H atom and an H^- ion. Metastable and long lived states of H_2^- have been previously observed by Kreckel et. al. [82] and Golser et. al. [83]. A table of expected mass spectrometer current values for different energy beams of H^- and H_2^- is shown in table 4.6 where all current values were calculated using equation 2.25 referencing an incident 30 keV H^- beam detected when 8.3 A of current is applied to the mass spectrometer dipole.

Initially, a 20 keV beam of H^- with a beam current of 3.5 mA ($\sim 170\mu$A after the collimator) was incident on the accelerator unit with 6 sccm of H_2 injected into the gas cell portion of the accelerator. The potential on the accelerator was set to 10 kV where, by table 4.6, it would be expected to see a signal of a newly formed H^- beam when up to 4.79 A of current was supplied to the mass spectrometer magnet. No signal of H_2^- was measured as there was a significant overlap with the primary beam but a suspected secondary beam of H^- was detected at a magnet current of 4.79 A and greater, this is summarized in table 4.7 and displayed in figure 4.5.

If the charge transfer reaction outlined in equation 4.4 were to take place it would be expected that the newly produced H^- beam would be measured at a current of 4.79 A and lower. This is because 4.79 A is the mass spectrometer current at which an H^- beam would be detected if it were to possess an energy of 10 keV. If the newly created

Table 4.6: Theoretical H^- and H_2^- beam energies versus mass spectrometer current for detection.

Accelerator Potential E_{H^-}/$E_{H_2^-}$ (kV)	**Mass Spec. Current I_{H^-} (A)**	**Mass Spec. Current $I_{H_2^-}$ (A)**
20	6.78	9.58
18	6.43	9.09
16	6.06	8.57
14	5.67	8.02
12	5.25	7.42
10	4.79	6.78
8	4.29	6.06
6	3.71	5.25
4	3.03	4.29
2	2.14	3.03

Table 4.7: The experimental parameters that were set for tests performed in figure 4.5 and the corresponding results. The non-zero beam current peak intensity was measured when 4.79 A was applied to the mass spectrometer dipole.

		Incident beam energy	
		20 keV	
		Incident beam current (before collimator/after collimator)	
		3.5 mA / 170 μA	
		Gas flow (sccm)	
		0	6
		Peak beam current intensity (nA)	
Accelerator potential (kV)	0	0.1<	0.1<
	10	0.1<	∼4

H^- ion is formed anywhere further downstream of the first electrode of the accelerator unit it would not be exposed to the full potential and exit the accelerating region at an energy lower than 10 keV. This would result in the newly formed H^- ion being measured at a mass spectrometer current lower than 4.79 A, whereas the opposite result is seen. This negative beam current measurement is only found when gas is injected into the accelerator unit and a potential is applied as seen by the control plot lines in figure 4.5. A lower accelerator potential of 7.3 kV was applied with the same incident beam parameters to observe the location of the secondary H^- beam, the results are plotted in figure 4.6.

The result of lowering the accelerator potential, again, produced an inverse measurement of what would be expected by the charge exchange hypothesized in equation 4.4. It should be noted that the shaded areas of figures 4.5 and 4.6 are where the secondary H^- beams are expected to be measured. More testing was carried out with different incident beam parameters, accelerator potentials, and gas flow values to determine how the secondary ion beam is being created and what kind of charge exchange is taking place. Experiments were performed using incident beam energies of 15 keV, 20 keV, and 25 keV at 3 mA whereas the accelerator potential was varied from 1 kV to 17 kV for each incident

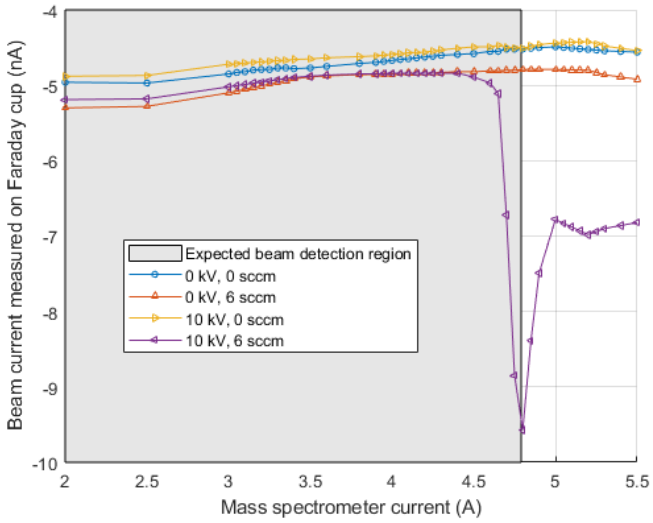

Figure 4.5: Current measured on the Faraday cup as a function of mass spectrometer current for the initial test of H^- beam on H_2 with 10 kV applied to the accelerator.

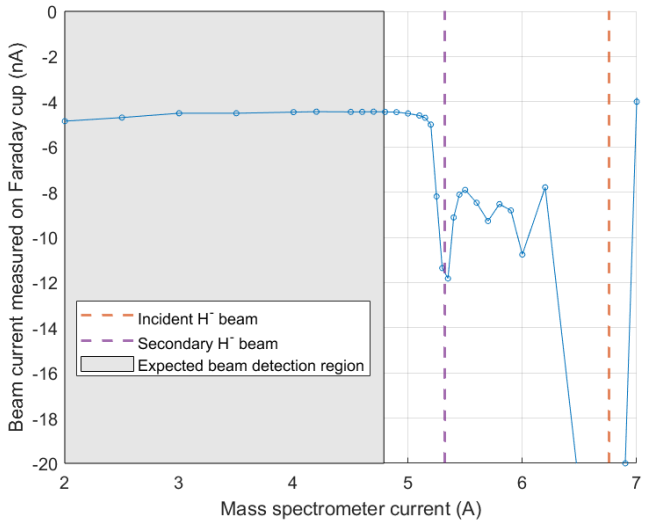

Figure 4.6: Current measured on the Faraday cup as a function of mass spectrometer current for the initial test of H^- beam on H_2 with 7.3 kV applied to the accelerator.

beam setting. The mass spectrometer magnet current was swept in order to locate the negative beam current peaks of secondary ion beams created. Figure 4.7 displays the mass spectrometer current location of negative beam current maxima for different accelerator potential values given the three different incident beam parameter configurations. These results are compared with the expected mass spectrometer current locations of secondary H^- beams that would be created through the charge exchange process of equation 4.4.

From these results it was hypothesized that the incident H^- beam was being slowed by the first electrode to a potential of V_B and colliding with the neutral gas within the gas cell which would neutralize a significant portion of the incident beam resulting in energetic neutral hydrogen beams passing through the accelerator. At some point throughout the beamline the energetic neutral would capture a free electron, negatively ionizing it again.

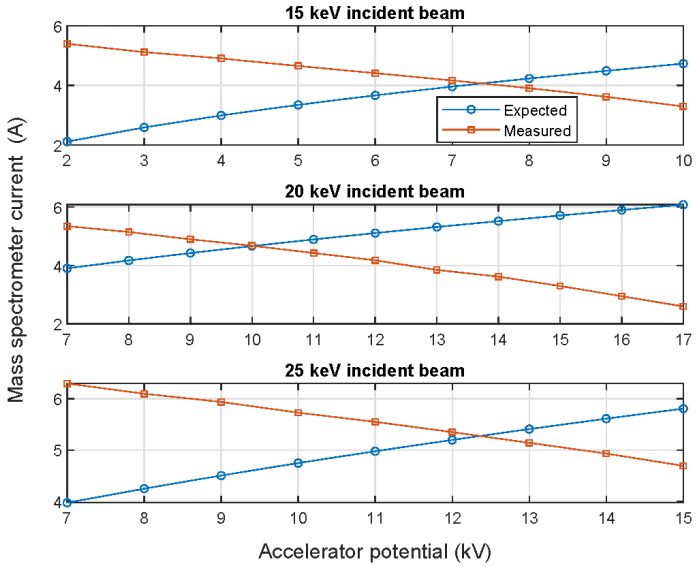

Figure 4.7: Mass spectrometer current location of negative beam current peaks for varying accelerator potential values and incident beam energies.

Equation 4.5 outlines the charge exchange of this slowed beam process.

$$H^-(V_B) + H_2 \rightarrow H(V_B) + H_2 + e \rightarrow H^-(V_B) + H_2 \tag{4.5}$$

The potential V_B is simply calculated by subtracting the incident potential by the potential of the first electrode. If the majority of the beam is neutralized at a potential of V_B and experiences electron reattachment after travelling through the accelerator beamline, the resulting beam current peak will be measured at a mass spectrometer current associated with an H^- beam with an energy of $E = V_B(eV)$. Figure 4.8 displays a plot of secondary negative ion beam current peak locations by mass spectrometer current using the same data from figure 4.7, but the potential at which the peaks are measured is adjusted to display the slowed beam potential V_B for each result. This is done in order to find the correlation between the charge exchange hypothesis outlined in equation 4.5 with the actual measurements.

The tail end of the beam current measurements trailing at mass spectrometer currents larger than the peak values shown in figures 4.5 and 4.6 likely represent the portion of energetic neutral H^- which recaptures an electron within the accelerator giving an additional acceleration to the beam which would be detected at a high mass spectrometer current. This tail on the beam current peak could also represent a beam which experiences neutralization further down the beamline so that it experiences some re-acceleration before being neutralized. This neutralized beam would still need to recapture a free electron after the accelerator in order to be detected on the Faraday cup after the mass spectrometer dipole magnet. In order to confirm that the beam being detected is a portion of the incident beam and not an ionized product of the neutral hydrogen which is injected into the accelerator, helium and argon were injected as the neutralizing target in an attempt to reproduce a similar result. Helium was chosen as a neutralizing gas as it was determined in section 4.1.1 that the conversion to a beam of He^- would have an extremely small cross-section that would not be measurable with a resolution of 0.1 nA. As for argon, there is only

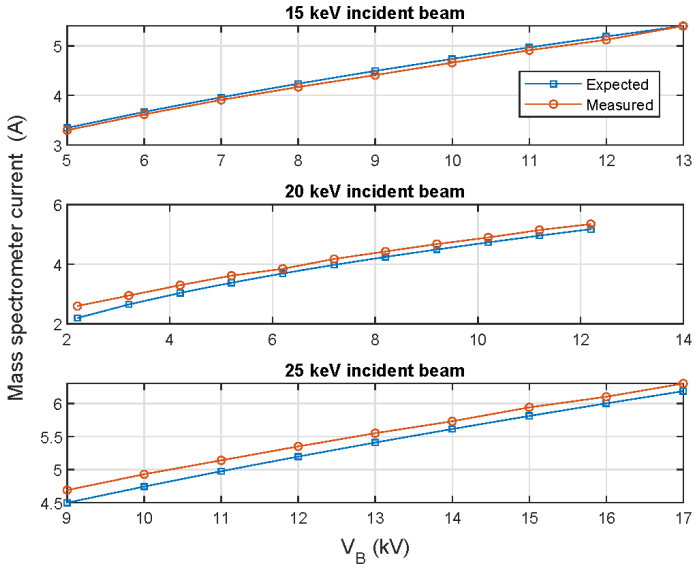

Figure 4.8: Mass spectrometer current location of negative beam current peaks for slowed beam values V_B at different incident beam energies.

one known metastable state which allows an electronic transition to produce Ar^-. Much like helium, this negative ion has only been formed through a double charge exchange collision with alkali vapour which allows a beam of Ar^+ to gain an electron reaching the metastable state that will accept another electron through collision, to transition to Ar^- [84]. Argon is also a very heavy gas in comparison to hydrogen so their negative ions would be well distinguished after mass separation. The results of this experiment are displayed in figure 4.9 which utilized the same incident beam parameters and accelerator potential values as the experiment shown in figure 4.5.

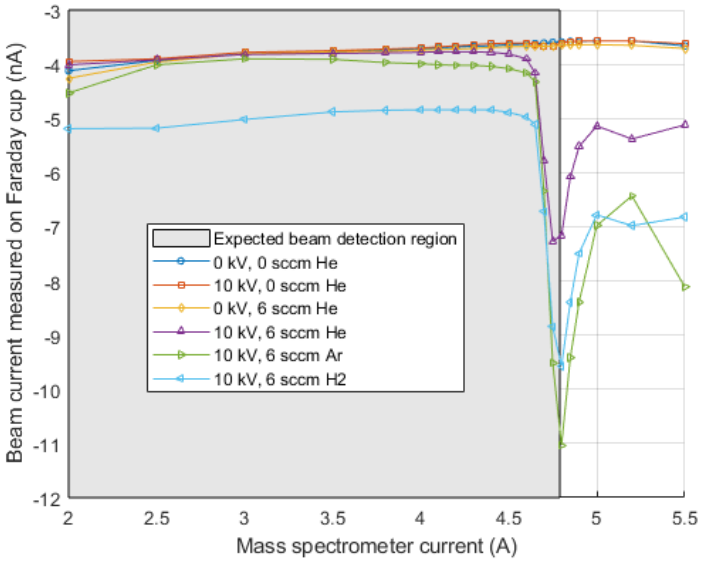

Figure 4.9: Current measured on the Faraday cup as a function of mass spectrometer current for test of 20 keV H^- beam at 3.5 mA on different neutral gases with 10 kV applied to the accelerator to display incident beam neutralization and electron reattachment.

It was found that the same mass spectrometer current was required to measure the beam current signal with 10 kV applied to the accelerator when hydrogen, helium and argon were injected into the gas cell portion. This result confirms that the negative beam current measurement is a product of the incident beam and not the neutral gas target.

It is likely that the charge exchanges outlined in equations 4.3 and 4.4 were not observed at a resolution of 0.1 nA on the picoammeter due to an off-resonance charge transfer resulting in a small cross-section. Both charge transfer reactions depend on the electron affinity of H_2 being close to the electron affinity of H as outlined in equation 2.6. As stated previously in this section, the electron affinity of H_2 is not well defined, thus it is likely that the difference in electron affinities is over 1 eV which would result in a cross-section too small to be detected by the equipment used for measurement (resolution of 0.1 nA).

4.1.3 H^- on CO_2

Another readily available, non-toxic compressed gas that was used as a target for H^- beams was CO_2. The hypothesized collisions which are based on known possible negative ion products from different methods [16], [18], [20], [87] are displayed in equations 4.6 to 4.11. The electron affinity of CO_2 is not well defined, with values recorded from calculations and experiments ranging from 2.2 eV to -1.2 eV [89] [90]. Some of the electron affinities listed could produce a near-resonant collision between CO_2 and the incident H^- beam. No other research is known of which impinges H^- beams onto CO_2, thus all charge exchange processes are theoretical.

$$H^- + CO_2 \rightarrow H + CO_2 + e \tag{4.6}$$

$$H^- + CO_2 \rightarrow H + CO_2^- \tag{4.7}$$

$$H^- + CO_2 \rightarrow H + C + O_2^- \tag{4.8}$$

$$H^- + CO_2 \rightarrow H + C^- + O_2 \tag{4.9}$$

$$H^- + CO_2 \rightarrow H + CO^- + O \tag{4.10}$$

$$H^- + CO_2 \rightarrow H + CO + O^- \tag{4.11}$$

CO_2 has an atomic mass of 44 AMU (atomic mass unit) making it the heaviest of the targets analyzed for negative ion production in this experiment. As a result, any heavy negative ions formed from the collision with H^- would require much larger mass spectrometer currents to be detected, even at lower energies. Table 4.8 includes the mass spectrometer currents required for detecting a list of possible negative ions and their corresponding energies dictated by the accelerator potential values. It should be noted that the negative ions that are included in table 4.10 are not listed in table 4.8.

Table 4.8: Theoretical CO_2^-, C^- and CO^- beam energies versus mass spectrometer current for detection.

Accelerator Potential $E_{CO_2^-/C^-/CO^-}$ (kV)	**Mass Spec. Cur. $I_{CO_2^-}$ (A)**	**Mass Spec. Cur. I_{C^-} (A)**	**Mass Spec. Cur. I_{CO^-} (A)**
20	44.76	23.38	35.71
18	42.46	22.18	33.87
16	40.04	20.91	31.94
14	37.45	19.56	29.87
12	34.67	18.11	27.66
10	31.65	16.53	25.25
8	28.31	14.78	22.58
6	24.52	12.80	19.56
4	20.02	10.45	15.97
2	14.15	7.39	11.29

Tests were performed with varying incident beam energies (15-30 keV), gas flow rates (0-9 sccm), and accelerator potential values (0-12 kV). It should be noted that higher accelerator potential values were used for some experiments but did not produce stable tests as multiple arcing events would take place throughout the sweep of the mass spectrometer current. Throughout all the experiments performed when injecting CO_2 into the gas cell, none of results produced the expected negative ion beam currents displayed in table 4.8 at a resolution of 0.1 nA. A summary of the experimental parameters used for all tests using CO_2 as a target are listed in table 4.9 with their corresponding beam current peak intensity results.

Table 4.9: Variable experimental parameters for tests with a carbon dioxide target and the corresponding beam current intensities associated with each combination of test settings.

		Incident beam energy (keV)			
		15	20	25	30
		Incident H^- beam current (mA)			
		1-6	1-7	1-10	1-11
		Gas flow (sccm)			
		0-9	0-9	0-9	0-9
		Intensity of peak measurement $\pm$ 0.1 (nA)			
Accelerator Potential (kV)	2	0.1<	0.1<	0.1<	0.1<
	4	0.1<	0.1<	0.1<	0.1<
	6	0.1<	0.1<	0.1<	0.1<
	8	0.1<	0.1<	0.1<	0.1<
	10	0.1<	0.1<	0.1<	0.1<
	12	0.1<	0.1<	0.1<	0.1<

Figure 4.10 shows a plot of the data collected with a 20 keV incident H^- beam with an accelerator potential of 6 kV and 6 sccm of CO_2 flowing into the gas cell. The shaded

region represents the mass spectrometer current range that any of the negative ions listed in table 4.8 would be detected if 6 kV is applied to the accelerator.

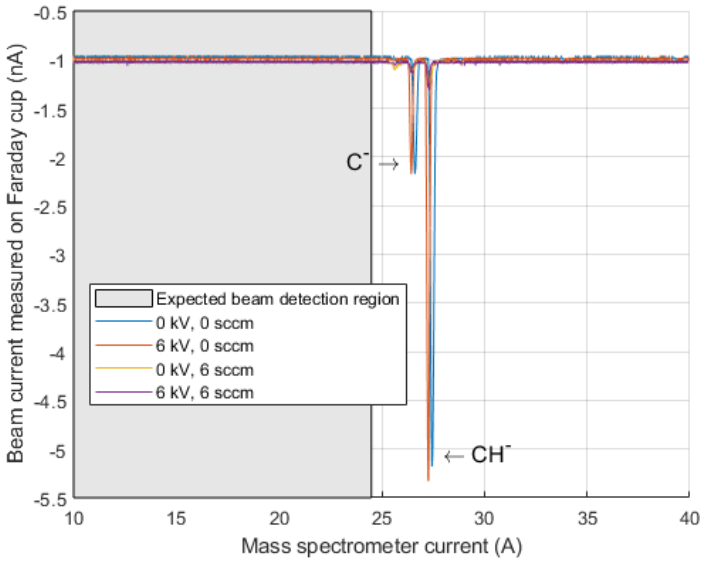

Figure 4.10: Current measured on the Faraday cup as a function of mass spectrometer current for 20 keV, 3 mA H^- beam incident on the gas cell with 6 sccm of CO_2 injected and 6 kV applied to the accelerator unit.

The two negative ion beam current peaks detected in the tests outlined by figure 4.10 show the products of contamination from previous experiments using the H^- ion source. An experiment performed in 2017 required the injection of Acetylene (C_2H_2) directly into the volume-cusp ion source on the ISTF in order to extract C^- beams from the plasma [88]. Even with extensive cleaning efforts it is still found that the ion source contains impurities and that some negative ion beams apart from H^- are still prevalent under normal operation. Using equation 2.25 it was calculated that the negative beam current peaks represent beams with mass numbers 12 and 13 corresponding to C^- and CH^- ions. The following plot (figure 4.11) is another example of the lack of negative ions detected from the predictions of equations 4.6-4.11 for different experimental parameters, it also displays the transmission of the C^- and CH^- beams in comparison to the flow of CO_2 into the gas cell. These contaminate peaks could be used in future experiments to characterize the mass spectrometer system along with scaling the current based on the primary H^- beam.

Most of the values for the electron affinity of CO_2 fall outside of the near-resonant charge transfer region (mass defect < 1 eV) in a collision with H^-. This would contribute to a small cross-section not detectable at a resolution of 0.1 nA on the measurement apparatus used for these experiments. The limited range of incident beam energy could also contribute to the lack of newly formed negative beam detection at 0.1 nA as the H^- velocity could fall within the adiabatic region, prohibiting an electronic transition, as explained in section 2.2.

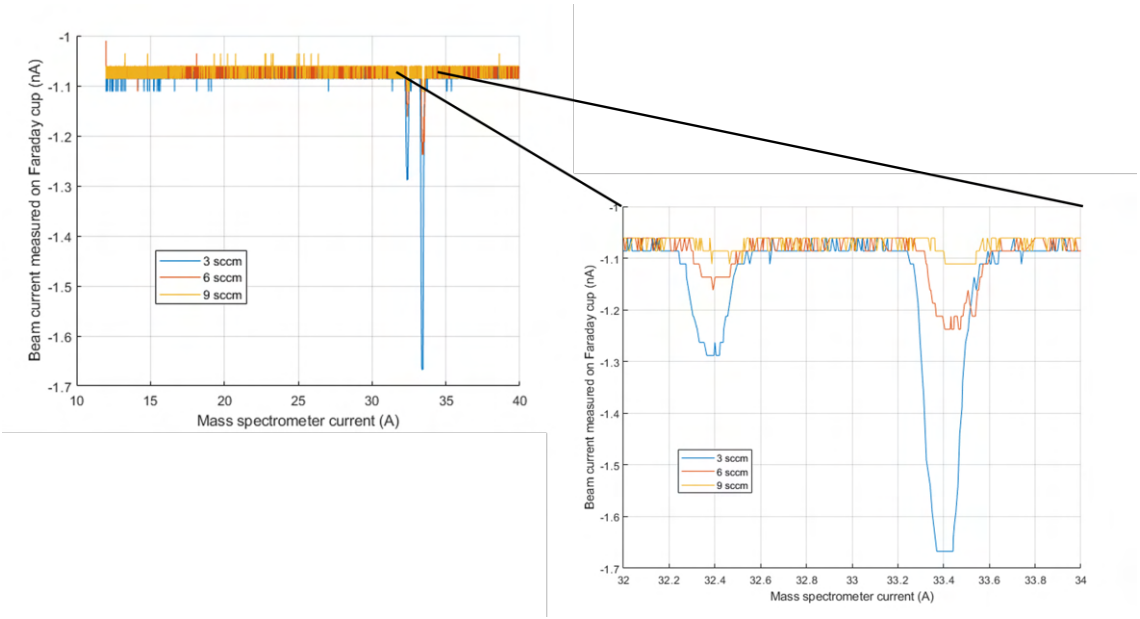

Figure 4.11: Current measured on the Faraday cup as a function of mass spectrometer current for 30 keV, 3 mA H^- beam incident on the gas cell with varying flow of CO_2 injected and 12 kV applied to the accelerator unit.

4.1.4 H^- on O_2

Further experiments were conducted using O_2 as a target gas. O_2 was chosen based on it's ability to form negative ions and it's availability and non-toxicity. The most recent measurement of the electron affinity of O_2 comes from Ervin et. al. which is stated as 0.448 ± 0.006 eV [85]. If H^- is incident on O_2, the difference in electron affinities between the projectile and the target is approximately 0.3 eV allowing for a near-resonant charge transfer. This is explained by equation 2.6 and creates the possibility for a larger cross-section reaction which could produce negative ion beams measurable at a resolution of 0.1 nA. The reason this gas was not tested before the previous targets was due to the availability of receiving the compressed gas and regulator equipment necessary for injection. Based on previous charge exchange studies, specifically the work done by Bailey and Mahadevan [16] which explores charge exchange between O^- ions and O_2 molecules at low energies (a few eV to 350 eV), the hypothesized charge exchange processes which could produce known negative ion structures are displayed in equations 4.12-4.14.

$$H^- + O_2 \rightarrow H + O_2 + e \tag{4.12}$$

$$H^- + O_2 \rightarrow H + O_2^- \tag{4.13}$$

$$H^- + O_2 \rightarrow H + O_2^{-*} \rightarrow H + O^- + O \tag{4.14}$$

The technique used for measuring any newly produced negative ion beams in this section of the experiment is the same as performed in sections 4.1.1, 4.1.2, and 4.1.3. A different mass spectrometer current range was analyzed as O^- and O_2^- ions are significantly heavier than ions produced from He and H_2 targets and lighter than some expected negative ions produced from CO_2. The mass spectrometer current range for detecting O^- and O_2^- beams with different energies is displayed in table 4.10. All expected mass

spectrometer current values are calculated using equation 2.25 using a 30 keV H^- beam detected at 8.3 A applied to the dipole magnet as a reference.

Table 4.10: Theoretical O^- and O_2^- beam energies versus mass spectrometer current for detection.

Accelerator Potential $E_{O^-}/E_{O_2^-}$ (kV)	**Mass Spec. Current I_{O^-} (A)**	**Mass Spec. Current $I_{O_2^-}$ (A)**
20	26.99	38.17
18	25.61	36.21
16	24.14	34.14
14	22.58	31.94
12	20.91	29.57
10	19.09	26.99
8	17.07	24.14
6	14.78	20.91
4	12.07	17.07
2	8.54	12.07

Again, it should be noted that the currents calculated for the corresponding energies in table 4.10 are the maximum values for expected beam current signal detection given this experimental setup. If negative ions are created further downstream within the accelerator unit they are subject to less acceleration and will result in lower energy beams that will be detected at lower mass spectrometer currents.

Initially, a 30 keV beam of of H^- at 6 mA (approximately 351 μA through the collimator) was incident upon the gas cell accelerator unit with 6 sccm of O_2 injected. It was found that 6 mA was an upper limit of the amount of current that could be deposited onto the collimator in order to keep the resistors used for the voltage division under their specified power and temperature ratings. It was found that even though the beam was being focused by the accelerator unit, some beam current was being deposited onto the electrodes and increasing the total current passing through the voltage division circuit. For extensive experiments periods upwards of 2 hours at high incident beam current values ($>$ 4 mA) it was found that significant damage to the first two resistors in the circuit closest to the collimator would occur. The expected regions for newly created negative ion beams, as outlined in table 4.10, were extensively investigated akin to the search for negative beam current peaks in the previous sections. The results of an initial test are displayed in figure 4.12 and it should be noted that the data points were recorded manually from the picoammeter. This was done in order to obtain a more concise signal as the sampling rate of the current measuring device was found to have difficulties capturing the full width of detectable beam current spikes when passed through a data acquisition device.

It is clear from figure 4.12 that a 1.6 nA peak of negative beam current is recorded in a region where O^- is expected to be detected at 6 kV when 6 sccm of O_2 is injected into the gas cell and 6 kV of potential is applied to the accelerator unit. Only under these conditions is the negative beam current peak measurable. With the incident H^- beam

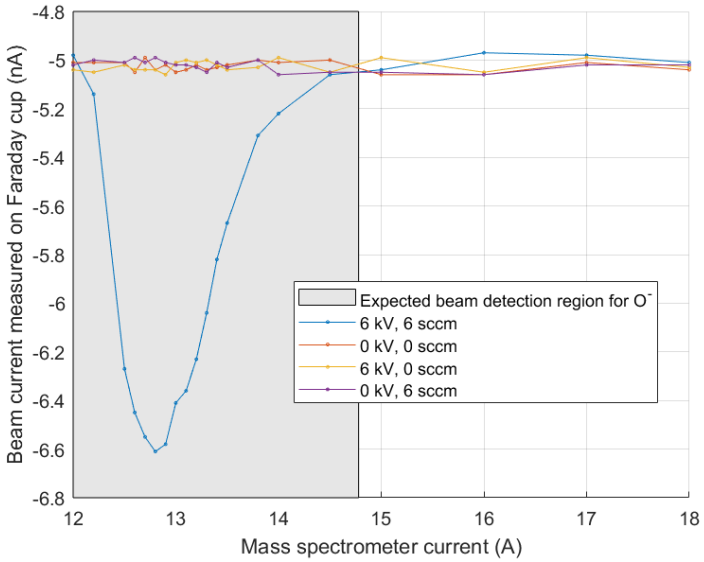

Figure 4.12: Current measured on the fixed Faraday cup as a function of mass spectrometer current for a 30 keV, 6 mA H^- beam incident on the gas cell with 6 sccm of O_2 injected and 6 kV applied to the accelerator unit with all control combinations of accelerator potential and gas flow.

conditions and O_2 injection flow rate fixed, the accelerator potential was adjusted to determine if the observed negative beam current peak shifted in relation to the accelerating potential applied. The potential was adjusted up to 12 kV where consistent measurements could be taken without frequent arcing events, the results are summarized in figure 4.13.

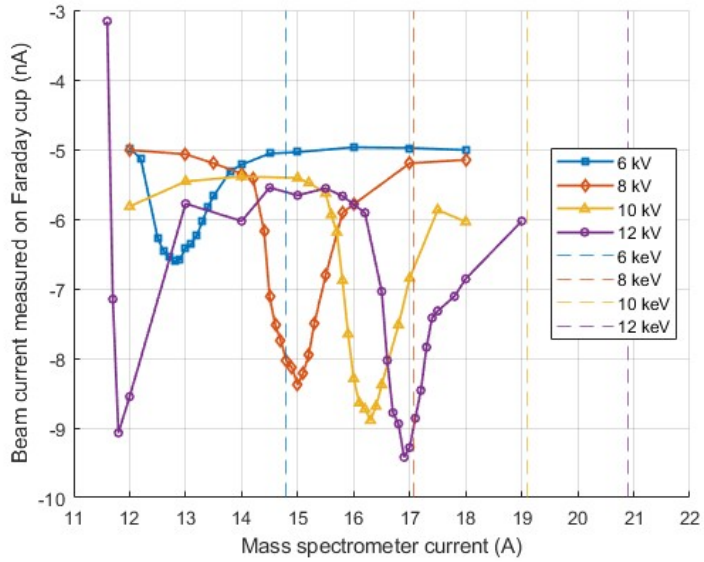

Figure 4.13: Current measured on fixed Faraday Cup as a function of mass spectrometer current for 6 mA H^- beam at 30 keV incident on 6 sccm of O_2 with varying accelerator potential values. The dotted lines indicate the mass spectrometer current at which a beam of O^- would be detected at the respective energies listed.

As expected, for newly formed negative ions in the gas cell unit, the negative beam current peak was measured at a higher mass spectrometer current value when a larger magnitude of accelerator potential was applied. The peaks are all located at a mass spectrometer current lower than the value of an O^- beam exposed to the full acceleration provided by the electrostatic accelerator, meaning that if the negative beam current being recorded is O^-, it is being formed further downstream of the first electrode of the accelerator unit. The gas flow injected into the accelerator unit was incrementally adjusted to find the optimal flow rate to produce the maximum amount of measurable negative beam current on the Faraday cup. The results of this test are summarized in figure 4.14.

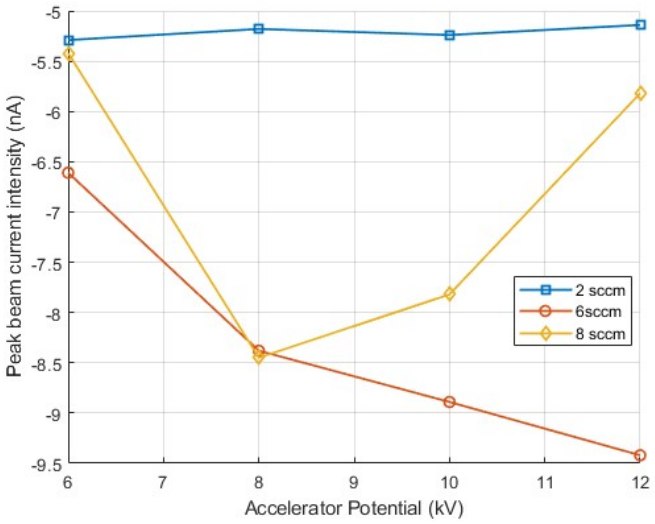

Figure 4.14: Peak beam current intensity measured on the fixed Faraday cup for different accelerator potential values for a 6 mA H^- beam at 30 keV incident on varying flow of O_2.

The optimal gas flow rate was found to be 6 sccm given the incident beam conditions. Based on the Molflow simulation of the ISTF this corresponds to an average pressure of 3.7 x 10^{-4} Torr within the electrostatic accelerator. It should be noted that at 4 sccm multiple arcing events occurred during testing which created disruptions in the measurement processes rendering the data unusable.

Drawing the attention back to figure 4.13, When the accelerator potential reached 12 kV another negative beam current peak was measurable approximately 5.1 A lower than the primary expected peak. This secondary peak could be the result of another charge state of the primary negative beam current peak (i.e. O^{2-}). By equation 2.25, it can be calculated that a 12 kV beam of O^{2-} would be detectable up to 10.45 A on the mass spectrometer dipole. Although this secondary negative beam current peak falls within this region of expected measurement, there is a limited amount of information available about the formation of O^{2-} and it's stability, thus, it can not be confirmed that this is the secondary peak being measured at this time. Another possible explanation for the secondary negative beam current peak is that the primary peak has a larger mass (O_2^-) or different isotope (^{17}O, ^{18}O) which is formed further down the beamline of the accelerating unit and the secondary peak is a lighter ion (O^-) which is also created near the last few electrodes of the electrostatic accelerator. Creation of negative ions from isotopes of

oxygen different from ^{16}O is unlikely seeing as ^{17}O and ^{18}O only make up 0.04% and 0.2%, respectively, of naturally occurring oxygen [86]. Based on the negative beam current peaks measured in figure 4.13, the following table displays the relation between the mass spectrometer current of the peak maxima, the potential applied to the electrostatic accelerator, the speculated beam species, and the energy in which the beam would have to posses in order to be measured at the given mass spectrometer current.

Table 4.11: Hypothesized beam species and energy of beam current peaks from figure 4.13.

Mass spectrometer current (A)	Accelerator potential (kV)	Hypothesized beam species	Beam energy (keV)
12.8	6	O_2^-	2.25
15	8	O_2^-	3.09
16.3	10	O_2^-	3.65
16.9	12	O_2^-	3.92
11.8	12	O^-	3.82

In a similar derivation to the sample values for the electrode potentials in the design of the charge exchange cell found in table 3.1, the electrode potential values for 6-12 kV profiles are calculated are displayed in table 4.12.

Table 4.12: Voltage profile of the electrodes for the accelerator unit with a varying potential applied.

Electrode Number	6 kV profile	8 kV profile	10 kV profile	12 kV profile
1	-6.00	-8.00	-10.00	-12.00
2	-5.88	-7.84	-9.80	-11.76
3	-5.51	-7.35	-9.18	-11.02
4	-4.90	-6.53	-8.16	-9.80
5	-4.04	-5.39	-6.73	-8.08
6	-2.94	-3.92	-4.90	-5.88
7	-1.59	-2.12	-2.65	-3.18
8	0	0	0	0

The location at which the ions would be formed in the electrostatic accelerator can be derived from the predicted beam energy in table 4.11. If the species of ion for each measured beam peak is the same as those listed in table 4.11, their corresponding beam energies would be between 2.25 keV and 3.92 keV. If the ions measured have a charge of -1, given the predicted beam energy for each potential profile, all of the negative ions collected at their specified beam current values would be created between electrodes 6 and 7. From table 4.12, it is seen that for each potential profile a beam energy of between 2.25 keV and 3.92 keV can only be obtained if the ions are formed between electrodes 6 and 7. The region for negative ion beam current detection was limited below 11 A on the mass spectrometer due to an inconsistent positive beam current flux detected. This phenomena is similar to the measurement limitations displayed in the highlighted region of figure 4.4. Due to this limitation, possible secondary beam current peaks are not detectable for

accelerator potentials that could be measured at values below 11 A when a 30 keV beam is incident on the accelerator. It was attempted to push the accelerator potential past 12 kV in order to further explore the nature of where the detectable beam current peaks are measurable and the spacing between peaks. It was found that arcing events were too frequent to record consistent measurements without self-protection of the accelerator power supply enabling and disrupting the data collection.

In order to further understand the measurement of multiple negative beam current peaks, the mass spectrometer current was fixed and the accelerator potential was adjusted up to the maximum range permitted by the power supply and accelerator unit. The goal was to see if multiple negative beam current signals were observed for the same mass spectrometer current which would indicate the possibility of multiple beam species being measured. This method was also found to reduce the number of arcing events by allowing for some arc discharge conditioning of the accelerator as the accelerator potential was increased. It was also easier to monitor the accelerator potential because it was the parameter which was actively being adjusted, if an arcing event were to occur the accelerator potential was quickly decreased so that the power supply would not trigger an automatic shut down. With the same incident beam conditions outlined in figures 4.13 and 4.14, tests were performed with the mass spectrometer current fixed at 15.5 A and 18.5 A. The results of these tests are shown in figures 4.15 and 4.16.

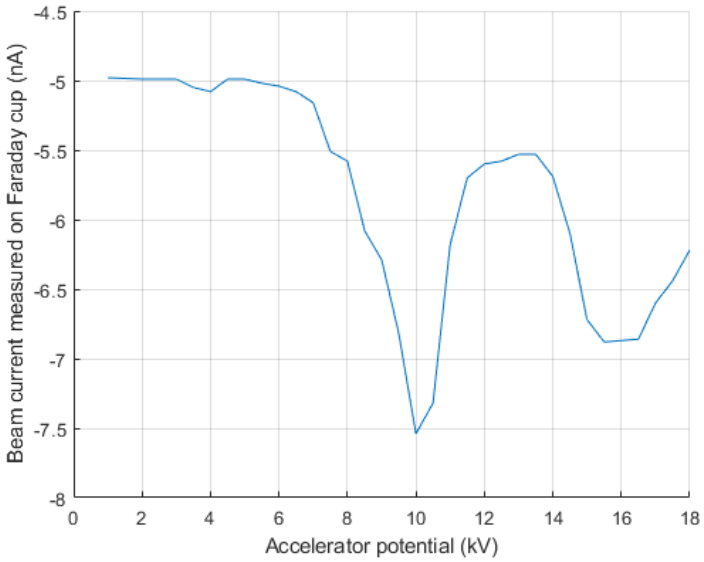

Figure 4.15: Beam current measured on fixed Faraday cup versus accelerator potential for 6 mA H^- beam at 30 keV incident on accelerator unit with 6 sccm O_2 injected with fixed mass spectrometer current of 15.5 A.

To determine the possible species of prominent peaks displayed in figures 4.15 and 4.16 the difference in the associated mass is found between the respective peaks. This is done by rearranging equation 2.25:

$$M_Y = \left(\frac{I_Y}{I_X}\right)^2 \frac{M_X E_X}{E_Y} \tag{4.15}$$

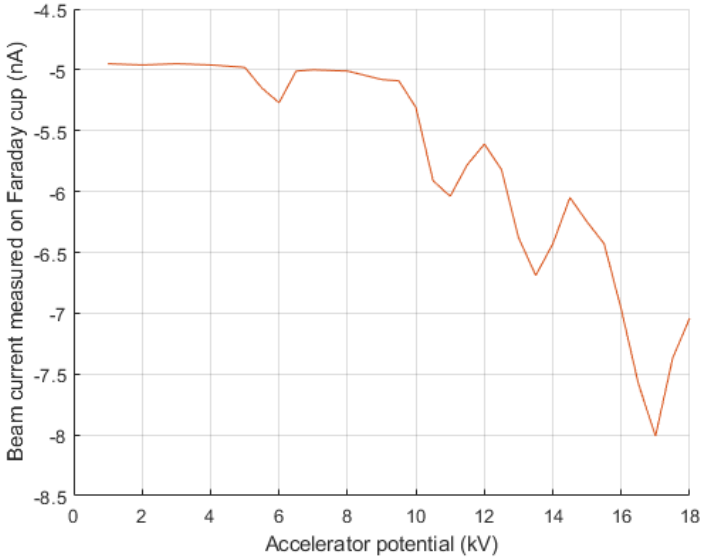

Figure 4.16: Beam current measured on fixed Faraday cup versus accelerator potential for 6 mA H^- beam at 30 keV incident on accelerator unit with 6 sccm O_2 injected with fixed mass spectrometer current of 18.5 A.

The values of I_X, M_X, and E_X are dictated by the incident H^- beam and are 8.3 A, 1 AMU, and 30 keV respectively. For the data in figure 4.16 the mass spectrometer current value I_Y is fixed at 18.5 A, while the beam energy E_Y is taken as 6 keV, 11 keV, 13.5 keV, and 17 keV based on the location of the negative beam current peaks. The resulting mass values are calculated to be 24.8 AMU, 13.5 AMU, 11 AMU, and 8.8 AMU respectively. Although these mass values do not equate the value of the expected negative ion species mass, it is possible that the beams are formed further downstream in the accelerator unit resulting in lower energies which would equate to more realistic mass values. Thus, the difference in these values is taken to further hypothesize the species that is being measured. The difference in mass between the 11 keV, 13.5 keV, and 17 keV peaks does not give a significant difference in mass and it is unclear whether these values are a different species or if it is the same species which is being created at different locations in the accelerator unit. However, the difference between the 6 keV and 17 keV peak is 16 AMU which equates to the difference in mass between O^- and O_2^- ions giving a possible theory the multiple negative beam current peaks detected. Using equation 4.15 to analyze the plot in figure 4.15, it was found that the difference in mass between the two energy peaks (10 keV and 16 keV) for a fixed mass spectrometer current of 15.5 A is approximately 4 AMU which is also the difference in mass between O^- and C^-. This calculation raises the question as to whether or not the O_2 being used for injection is adequately pure for testing. For the tests using O_2 for injection, up until this point in the experiment, a bottle of 99.5% O_2 was injected that was primarily used for welding purposes. The O_2 gas line usually shares a gas line with acetylene (C_2H_2), and even though the primary gas line was changed for the experiments, there could possibly be some contamination which is occurring to inject different species other than O_2 into the charge exchange cell.

High purity (99.999%) O_2 was acquired to perform more tests and reduce the possibility of contamination in the charge exchange cell. Again, a 30 keV H^- beam with a beam current of 6 mA was incident on the charge exchange cell with high purity O_2

injected at 6 sccm. Tests performed with the less pure O_2 were recreated to compare the results with the high purity gas target. The mass spectrometer current was swept over the expected negative ion detection region for different accelerator potential values, the same technique which produced the data for the plot in figure 4.13. The results of these tests are summarized in figure 4.17.

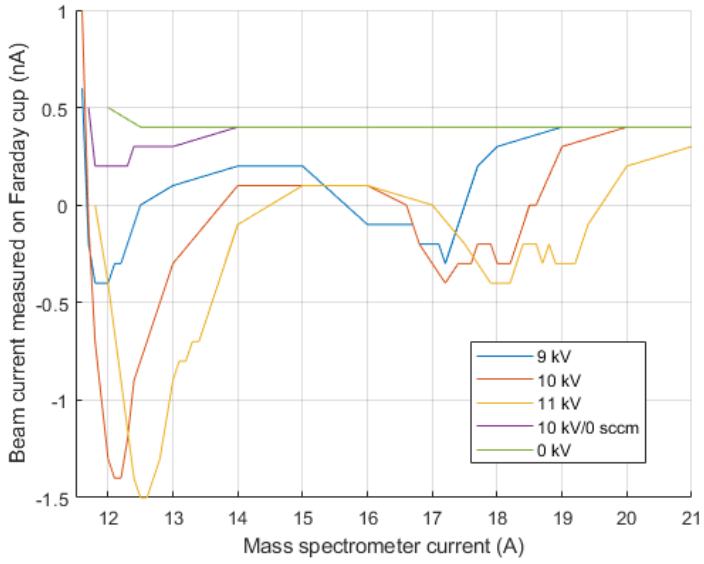

Figure 4.17: Current measured on the fixed Faraday cup as a function of mass spectrometer current for 6 mA H^- beam at 30 keV incident on the accelerator unit with 6 sccm high purity O_2 injected with varying accelerator potential values.

It was found that the intensity of the beam current measured with the high purity O_2 was smaller than the tests recorded with the 99.5% O_2. The negative beam current signals were only measurable when accelerator potentials between 9 kV and 11 kV were applied with O_2 injected into the accelerator unit. Multiple peaks were still detected which increase in detected mass spectrometer current when the accelerator potential is increased. When comparing figure 4.17 plot with figure 4.13, it is found that the negative beam current peak locations are not identical for similar accelerator potential values. This discrepancy leads to the belief that damage to the accelerating circuit may have occurred over the course of one or both of the tests even with periodic maintenance of the charge exchange cell between experiments. This damage is likely from high incident beam current tests which drove the resistors being used above their maximum power specifications. This discrepancy could also be a product of hysteresis in the electromagnet, although this is just a speculation and further tests would need to be performed to confirm this.

The continuation of research in the area of H^- on O_2 to produce negative ions was concluded for this project as the experiments performed with limited time did not reach a definitive answer as to what species of ion were being measured on the Faraday cup at a resolution of 0.1 nA. However, negative beam current signals were measured under conditions where O_2 was injected into the gas cell and potential was applied to the accelerator unit. These signals were not measured under conditions where a gas target was not injected and potential was not applied to the accelerator, implying that some negative ions were created under the experimental conditions of this section. The mass spectrometer

current range which was used to detected these negative beam current signals was well above the maximum value for H^- measurement at 30 keV which clearly distinguishes the signals from the beam provided by the source. The limitations of the project timeline and design of the charge exchange cell were the factors that halted any further efforts to explore this area. This section of the project was an extension of the initial goal to create negative helium ion beams through charge transfer, it is viewed as a good starting point for insight into future research which could be carried out in this area of study. Of the gases used for targets of H^- beams, O_2 has the highest theoretical probability of successful charge transfer. The energy defect between the projectile and target for this collision is within 1 eV, classifying it as near-resonant, and the target is known to produce multiple negative ions through other charge exchange methods. Without knowing the species or reasoning for the multiple peaks measured across the mass spectrometer current scans we will report a conversion rate between H^- and the O_2 gas target to some negative ion beam X^-. The maximum intensity of the beam current peaks was 4 nA with a 30 keV incident H^- beam with 12 kV applied to the accelerator unit and 6 sccm of O_2 injected into the gas cell portion of the accelerator. The indecent H^- beam current on the collimator was 6 mA which translates to 351 μA of beam entering the accelerator unit. Thus, a conversion of 0.00114% from H^- to X^- could be reported if the ion beam species could be confirmed. Improvements to the charge exchange cell and possible directions for continued work will be discussed in section 5.1.

Chapter 5

Conclusions

The goal of this thesis intended to explore the formation of negative ions from neutral gases through the process of charge transfer by developing a new method that did not involve the use of alkali or other metallic vapours, the commonly used hazardous charge exchange medium. The experimental method utilized a novel idea extended from the work of Doupé and Litherland which involved leveraging a D-Pace TRIUMF licensed H^- ion source to impinge beams onto a charge exchange cell containing a neutral gas target. The proposed idea was that the incident H^- beam would transfer an electron to the target neutral gas (X) which would be accelerated to create beams of X^-. The first target neutral gas chosen for study was helium with the intention of producing negative helium ions (He^-) through this method. The measurements of these collisions carried out using the novel method are a first of their kind. Although the charge transfer from H^- beams to He gas is theoretically unlikely due to the target residing in a state which is not known to allow for electronic transition to He^-, because of the industrial importance of the newly formed He^-, this was the first neutral gas target studied.

The charge exchange cell used for conducting this method was designed and constructed specifically for this project and included an in-vacuo electrostatic accelerator with semi-contained region for the gas target injection which, on its own, was an important achievement of this thesis.

The charge exchange cell was placed in the beamline of the Ion Source Test Facility (ISTF) at D-Pace which is equipped with a TRIUMF licensed H^- ion source, a mass spectrometer electromagnetic dipole with adjustable entrance and exit slits that were fixed at 2 mm for the duration of the experiments performed for this project, and a fixed Faraday cup for beam current collection after mass separation. The resolution of beam current measurement was 0.1 nA recorded using a Keithley picoammeter. Previous work in this area of study showed that acceleration and measurement of newly created negative ion beams from neutral gas targets was achievable. These studies stated that under certain conditions, minimizing the energy defect of a collision can create near-resonant charge exchange conditions resulting in larger cross-sections.

Using helium as a target was believed to have near-resonant conditions based on the electron affinity of metastable He^- (0.08 eV) in comparison to H^- (0.75 eV). An estimated total electron cross-section calculation produced results between 5.34 x 10^{-15} cm^2 and 1.79 10^{-14} cm^2 which could result in the inclusion of a charge transfer cross-section

producing He^-. Although, this approximation was coupled with rather large errors from estimating the length of the gas target and the temperature of the collision region. Helium was injected into the charge exchange cell at varying flow rates with incident H^- beam parameters ranging from 15-30 keV and 0-11 mA. The potential applied to the accelerator was also varied in order to find optimal collision parameters. Through extensive experimentation, no signal of He^- was measured at a resolution of 0.1 nA. Further literature research suggests that He^- is only formed from an excited state of helium $(1s2s)^3S$ and it is suspected that the majority of the gas target is in the ground state $(1s^2)^1S$ which does not allow transition to the metastable He^- state.

Given the extensive development that had been put into the design and construction of the charge exchange cell and all components associated with the experimental setup, it was decided that the limited timeline of the project would be used to study the collision of H^- on different gas targets using the same experimental setup. H_2, CO_2 and O_2 were chosen as gas targets as they are non-toxic, readily available, and have to potential to create negative ions through near-resonant charge transfer.

The purpose of impinging H^- on H_2 was a proof-of-concept for the charge exchange cell and an exploration of accelerating newly formed negative ions from an H_2 gas target which has not previously been studied using this method of incident negative beams on neutral gases. It was found that negative beam current signals were measured outside of the expected detection regions for newly produced negative ions. It was hypothesized that a negative beam produced with this method of charge exchange would be measured on the Faraday cup at higher mass spectrometer currents as the accelerator potential was increased, but what was recorded was the opposite effect. It was found that the H_2 gas would strip the incident H^- beam of its electron, creating an energetic neutral. The energy of the resulting neutral hydrogen beam was dictated by the accelerator potential, the larger the potential the greater the deceleration of the incident beam. Some of the neutral hydrogen beam would regain an electron at some point before reaching the mass spectrometer dipole, giving the ion a negative charge and allowing the slowed beam to be measured on the Faraday cup.

The magnitude of these slowed beams was measured up to 5 nA on the picoammeter. Although this charge transfer was not the hypothesized single step exchange, these measurements are a new result which have not been previously recorded in literature.

The maximum detectable beam current was measured with a 30 keV H^- beam at 6 mA incident on the charge exchange cell with 6 sccm of argon injected into the gas cell. Argon acted as a better stripping gas likely due to its mass and inert nature. The energy defect of this collision is not well defined but the most recent studies suggest that it would be close to 1 eV which could classify a possible charge exchange as non-resonant creating a cross-section too small to measure negative ion beams at a resolution of 0.1 nA.

The next gas chosen for study was CO_2 as there are many known negative ions which could possibly be a product of the gas target. However, no negative ion beam currents were detected at a resolution of 0.1 nA when varying all parameters listed in table 4.9 that would be possible products of the CO_2 target. Negative ion beams of C^- and CH^- were measured but only due to the overlap with the mass spectrometer current range which was

being analyzed for this set of experiments. The C^- and CH^- beams are a result of a small amount of contamination in the source and are measured under normal operation without the use of the charge exchange cell or a gas target. The inability to detect ion beams that are a product of the CO_2 target at a resolution of 0.1 nA is likely due to the off-resonance of the collision which stems from an energy defect above 1 eV. The electron affinity of CO_2 is not well defined and thus it is likely further from the electron affinity value of hydrogen which would result in a small charge transfer cross-section.

Finally, O_2 was used as a gas target within the charge exchange cell. O_2 has a well defined electron affinity of 0.448 eV, resulting in an energy defect of less than 1 eV when colliding with an H^- beam which creates the possibility for near-resonant charge transfer. With O_2 used as a target, it was found that some negative beam current was measured at a magnitude of up to 4 nA within the mass spectrometer current ranges that the product negative ions of O_2 would be expected. The maximum negative beam current production was measured with a 30 keV H^- beam at 6 mA incident on the charge exchange cell with 6 sccm of O_2 injected into the gas cell portion and 12 kV applied to the accelerator unit. Unlike the tests performed with H_2, these negative beam current signals were found to shift with the accelerator potential, suggesting that the signals were products of ions formed within the charge exchange cell. Multiple negative beam current signals were measured for certain incident beam and charge exchange cell parameters which lead to the hypothesis that different charge states or species might be formed in the gas cell. Further experiments were performed including the use of high purity O_2 in an attempt to determine the species of the current being measured on the Faraday cup but no further conclusions were drawn given the time and technical limitations of this project.

The conversion rate between the incident H^- beam and the resulting X^- beam produced from an oxygen target is up to 0.00114%.

The following section includes suggestions on improvements that could be made to this experiment and ideas for future research in this area of study which may be useful to anyone who would like to pursue this topic.

5.1 Future work

Since the 1980's, the development of new methods for negative ion production has drastically slowed down, leaving opportunity for exploration in this field. This project showed potential in the formation of negative ion beams through non-traditional methods which could be researched further with improvements to the experiment.

In terms of the experimental setup, the main limitations existed within; the H^- ion source used for creating incident negative beams, the design and durability of the charge exchange cell, and the sensitivity of the current measuring equipment.

The D-Pace TRIUMF licensed H^- ion source offered a good range of beam parameters for an introduction to this type of work but as described by Massey, near and non-resonant collisions are heavily dependent on the incident beam energy [26]. This could be a limiting factor if the optimal collisional energy for these types of charge transfer reactions is orders of magnitude different from the tens of keV range that the D-Pace H^-

source offers. Modifications to the H^- source or the use of multiple different ion sources resulting in a larger range of incident energies could produce measurable results for some collisions which would not produce a high cross-section reaction otherwise.

The charge exchange cell was designed with electrical breakdown considered, but in practice, arcing events were found to be a large contributor in the limitations of experiments performed. A redesign of the charge exchange cell would focus on creating a larger gap between the electrodes without compromising the focusing thin lens effect. The shape of the insulators used for electrode isolation would also be considered and possibly reconfigured in order to eliminate high concentrations of electric fields near the electrode junctions [91]. These adjustments to the accelerator design would likely require a larger vacuum box in order to increase the distance between electrodes without eliminating a larger number of electrodes in order to keep a smooth and focusing acceleration of the beams. Ultimately, a more extensive optimization of the optics of this electrostatic accelerator should be preformed using simulation if further experiments are to be conducted. The capabilities of SIMION were not fully taken advantage of and this likely had a great effect on the ability to produced measurable beams of negative ions. More simulations should be performed with different gas targets for future experiments in order to understand the space charge effect of the newly formed beams and varying residual gas pressures. Simulation should also be performed in order to confirm that the accelerator unit has an overall focusing effect which would not result in a large beam loss between the end of the charge exchange cell and the end of the beamline. For changes such as varying the gap between electrodes and varying the number of electrodes, simulations would be paramount to the understanding of the ion optics. The damage to the resistors which provided voltage division between the electrode was also found to be a drawback to the electrostatic accelerator design. Exposure to the incident H^- beam degraded these resistors which led to component failure in some instances. A solution to this issue would be to design an external, well insulated circuit that would not be in vacuum or exposed to any particle beams. Vacuum feed-through ports would supply the potential to each electrode from the circuit. The size of this circuit could be much larger and use higher power rated resistors which would not be damaged when high power H^- beams were incident on the electrodes. A more in depth full thermal simulation of the entire accelerator unit could be performed for high beam power situations which would give insight on how temperature resistant the components used for construction must be. This thermal simulation would also give a more accurate temperature approximation of the region in which negative ions are produced which would reduce the error on cross-section estimations like the one performed for a helium target.

The use of more sensitive beam current measuring equipment could result in the detection of negative ion beams which would be measured at a smaller resolution than the current value of 0.1 nA. The Keithley picoammeter used for this experiment claims to have a capable resolution of 10 fA, but the noise present under the operation of the experiment made such a resolution unachievable. Further efforts could be made to eliminate all electrostatic coupling and stabilize the temperature of the charge exchange cell in order to reduce an offset drift current which could contribute to the high noise floor. With improved beam optics (as mention in sections above) and pumping capabilities of the test setup, more beam transmission could be achieved which could allow for the present current resolution to detect some newly formed negative ion beams. For future experiments,

the adjustment of the mass spectrometer entrance and exit slits should be utilized to improve the resolution between ion species and ions of differing momentum values.

Any future research on this topic could be carried out in multiple directions. The original intent of producing negative helium ions through collisions with H^- beams and a helium gas target has potential for further exploration. Based on the results of the tests performed in this project and the understanding of the theory of negative helium ion production, an effort could be made to excite the neutral helium gas target to allow for effective charge transfer. An electron gun or heater could be implemented onto the injected helium gas which could possibly excite the target to the $(1s2)^3S$ state. Different incident negative ion beams could also be tested which could result in a lower energy defect for the collision and lead to a higher charge transfer cross-section. Seeing as He^- is a metastable ion, the length of the beamline could be shortened in order to reduce the chance of electron auto-detachment or detachment through collision with other gas atoms and the ion optics of the shortened beamline could be optimized using SIMION. Both the incident H^- and helium target are light species and would not require the large magnetic field strength available from the mass spectrometer dipole used in this experiment. Thus, a smaller magnet closer to the charge exchange cell could be leveraged in order to separate the two species and possibly measure beams of He^- if they were formed at a relatively significant conversion rate.

With an extended project scope, the results from experiments performed with O_2 could be further investigated in order to determine the nature of the signals which were measured. The improvements to the current experimental setup which are mentioned above would greatly increase the possibility of gathering more data for this collision. The improvements to electrical breakdown resistance of the accelerator unit would allow for a larger range of potentials to be applied to the accelerator with fewer arcing events. This would give further insight into the correlation between the mass spectrometer current at which the negative beam current signals were measured and the accelerator potential of the system. Improved beam optics and a more sensitive current measuring system with a higher sampling rate could allow for higher resolution signals to be recorded, which would be of particular importance to experiments with low intensity signals such as those using high purity O_2.

This project provided a great introduction into the world of ion production and many important lessons were learned along the way. There is still lots of work to be done in this area of study and many uncertainties to be explore. I hope that the research done for this project can positively contribute to the understanding of this field.

Bibliography

[1] I. Ahmad, F.I. Ezema, *Ion Beam Applications*, IntechOpen (2018), pg. 3-9.

[2] M. Budnar, P. Pelicon, *Research at the Tandem Accelerator*, Nuclear Energy in Central Europe (1998), pg. 59-65.

[3] International Atomic Energy Agency, *Instrumentation for PIXE and RBS*, IAEA-TECDOC-1190.

[4] J.F. Wacker et. al., *Accelerator Mass Spectrometry*, Encyclopedia of Spectroscopy and Spectrometry (Third Edition), Academic Press, (2017) pg/15-17.

[5] J. Ishikawa, *Ion sources for industrial applications (invited)*, Reveiw of Scientific Instruments (1998) vol. 69, num. 2

[6] J.S. Williams, *Ion implantation of semiconductors*, Material Science and Engineering: A, (1998) vol. 253, num. 1-2, pg. 8-15.

[7] S.B. Felch, *Ion implantation for semiconductor devices: The largest use of industrial accelerators*, Proceedings of PAC2013, (2013), pg. 740-744.

[8] S. Chang et. al., *High Energy Hydrogen and Helium Ion Implanter*, Applied Materials, Varian Semiconductor Equipment (2014).

[9] I.G. Brown, *The Physics and Technology of Ion Sources - Elementary Ion Sources*, WILEY-VCH (2004), pg. 7-29.

[10] M. Bacal, M. Sasao, and M. Wada, *Negative Ion Sources*, Journal of Applied Physics **129** (2021) no. 22.

[11] J. Ishikawa, I.G. Brown, *The Physics and Technology of Ion Sources - Negative Ion Sources*, WILEY-VCH (2004), pg. 285.

[12] M.I. Current, H. Ryssel, *Ion Beam Purity and Wafer Contamination*, Microcontamination (1994), ch. 12, pg. 1-35.

[13] V. Dudnikov, *High intensity source of He negative ions*, 6th International Particle Accelerator Conference (IPAC) (2015).

[14] T. Kuo, et. al., *On the development of a 15 mA direct current H^- multicusp source*, Review of Scientific Instruments, (1996), **67(3)**.

[15] J.P. Doupé, A.E. Litherland, *An electron-transfer gas ion source with isobar seperation for Cl^-*, Nuc. Inst. and Meth. in Phys. Res. B 259 (2007) pg. 217-223

[16] T.L. Bailey, P. Mahadevan, *Electron Transfer and Detachment in Collisions of Low-Energy Negative Ions with O_2^**, The Journal of Chemical Physics (1970), vol. 52, num. 1.

[17] J.B. Hasted, R.A. Smith, *The detachment of electrons from negative ions*, Proceeding of the Royal Society A (1956), vol. 235, num. 1202.

[18] E.E. Muschlitz Jr., J.H. Simons, *The measurement of electron exchange in gases at low pressure*, Journal of Physical Chemistry (1952), vol. 56, num. 7.

[19] J.N. Bardsley, *Electron detachment and charge transfer in H-H^- collisions*, Proceedings of the Physical Society (1967), vol. 91, num. 2.

[20] S.K. Gupta, C.E. Melton, *Charge transfer reaction between oxygen and H^- from water*, Journal of Chemical Physics (1974), vol. 61.

[21] V.A. Esaulov et. al., *Electron detachment and charge exchange to shape resonances in H^- collisions*, Journal of Physics B (1984), vol. 17.

[22] D.R. Nicholson, *Introduction to plasma theory*, Wiley (1983).

[23] G.D. Alton, *Electrostatics Accelerators*, *Springer* (2005), pg. 222-273.

[24] I.G. Main, *Negative helium ions for tandem accelerators*, Physics Bulletin 20 (1969), pg. 419

[25] J.R. Peterson, D.C. Lorents, *Total Charge-Transfer Cross Sections for He+ and Ar+ on K, Rb, and Cs: Near-Resonant Reactions Leading to Excited Final States**, Physical Review (1968) vol. 182, num. 1

[26] H.S.W. Massey, *Collisions between atoms and molecules at ordinary temperatures*, Reports on progress in physics (1949), vol. 12, 248

[27] I.M. Fogel et. al., *On the applicability of Massey's adiabatic hypothesis to double charge exchange*, Soviet Phyiscs Jetp. (1959), vol. 35, num. 3.

[28] W. Grüebler et. al., *Charge exchange collisions between hydrogen ions and alkali vapour in the energy range of 1 to 20 keV*, Helvetica Physica Acta (1970).

[29] A.V. Bunge, C.F. Bunge, *Electron affinity of helium $(1s2s)^3S$*, Physical Review A (1979) vol. 19, num. 2

[30] O. Goscinski, B.T. Pickup, *Direct calculation of ionization energies. Transition operator for the ΔE_{SCF} method*, Chemical Physics Letters (1973) vol. 22, num. 1

[31] J.B. Hasted, A.R. Lee, *The Near-adiabatic Criterion in Charge Transfer Collisions*, Proc. Phys. Soc. (1962), vol. 79, pg. 702-709.

[32] D.C. Harris and M.D. Bertolucci, *Symmetry and Spectroscopy, An Introduction to Vibrational and Electronic Spectroscopy* Dover Publications, Inc., New York. (1989).

[33] A. Einstein, *Relativity the Special and General Theory*, Henry Holt and Company (1920).

[34] N. Pichoff, *Introduction to RF Linear Accelerators*, CERN Accelerator School, pg. 105-128.

[35] F. Hinterbeger, *Ion optics with electrostatic lenses*, CAS - CERN Accelerator School : small accelerators (2006), pg. 27-44.

[36] D.A. Edwards, M.J. Syphers, *An Introduction to the Physics of High Energy Accelerators*, WILEY-VCH (1993), pg. 78-85.

[37] E. Bravin, *Transverse emittance: CAS - CERN Accelerator School: Beam Instrumentation*, Proceedings of the 2018 course on beam instrumentation for particle accelerators (2018) pg. 14.

[38] M. Ferrario, et. al., *Space Charge Effects*, INFN-LNF and Universrity of Rome (2016).

[39] V. Dudnikov, *Development and Applications of Negative Ion Sources*, Springer Series on Atomic, Optical, and Plasma Physics (2019) vol. 110, pg. 7

[40] H. Wiedemann, *Particle Accelerator Physics*, Springer (2007), pg. 39

[41] N. Marquardt, *Introduction to the Principles of Vacuum Physics*, Institute for Accelerator Physics and Synchrotron Radiation, pg. 1.

[42] A. Chambers, *Modern Vacuum Physics*, Chapman & Hall/CRC (2004).

[43] K. Jousten, *Gauges for fine and high vacuum*, Physikalisch-Technische Bundesanstalt (2007).

[44] K. Jousten, *Ultrahigh vacuum gauges*, Physikalisch-Technische Bundesanstalt (2007).

[45] P. Grafström, *Lifetime, cross-sections and activation*, CERN (2007).

[46] J. Ish, et. al., *Electron detachment cross-sections in low energy heavy negative ion beam apparatus*, Vacuum (1989), vol. 39, pg. 1127-1130.

[47] W.J. Lichtenberg, et. al., *Electron-loss cross sections for negative ions at high energies*, J. Phys. B: Atom. Mol. Phys. (1980), vol. 13, pg. 343.

[48] *D-Pace*, https://www.d-pace.com/

[49] J.L.R. Hayden, *The dielectric strength of the vacuum: Electrostatic ionization gradient of metal electrodes*, Journal of the American Institute of Electrical Engineers (1922), vol. 41, num. 11.

[50] F. Paschen, *Ueber die zum Funkenübergang in Luft, Wasserstoff und Kohlensäure bei verschiedenen Drucken erforderliche Potentialdifferenz*, Annalen der Physik (1889), vol. 273, num. 5.

[51] A.A. Martins, M.J. Pinheiro, *On the propulsive force developed by asymmetric capacitors in a vacuum*, Physics Procedia (2011), vol. 20, pg. 112-119.

[52] *Onshape®*, https://www.onshape.com/en/

[53] K.C.A. Smith, *Electrical circuits: an introduction*, Cambridge University Press (1992).

[54] *The Engineering Toolbox: Electrical Conductivity - Elements and other Materials*, https://www.engineeringtoolbox.com/

[55] *McMaster-Carr - Plastics*, https://www.mcmaster.com/products/plastics/

[56] *Vishay Intertechnology*, https://www.vishay.com/

[57] *SIMION*, https://www.simion.com/

[58] *Brooks Instruments GF40 Mass Flow Controller*, https://www.brooksinstrument.com/

[59] *LabVIEW*, National Instruments, https://www.ni.com/

[60] *6485 Keithley picoammeter*, https://www.tek.com/en/products/keithley/

[61] R. Johnston, et. al., *Realization of a Large-Acceptance Faraday Cup for 3 MeV Electrons*, Physics. ins-det (2018).

[62] H. Fernandes, et. al., *Design and Testing of Faraday's Cup for NSLS-II LINAC and Booster**, Proceedings of PAC2013 (2013).

[63] R.A. Buerschaper, *Thermal and Electrical Conductivity of Graphite and Carbon at Low Temperatures*, Journal of Applied Physics (1944), vol. 15, pg. 452-454.

[64] *McMaster-Carr - Graphite*, https://www.mcmaster.com/products/graphite/

[65] *SolidWorks®*, https://www.3ds.com/products/solidworks

[66] *FEMM*, https://www.femm.info/

[67] L. Reimer, *Emission of Backscattered and Secondary Electrons*, Scanning Electron Microscopy, pg. 135-169.

[68] *Samarium Colbalt Data Sheet*, Bunting Magnetics Europe, https://www.bunting-berkhamsted.com/

[69] *WRG-S-NW25*, https://shop.edwardsvacuum.com/products/d14701000/view.aspx

[70] J. Shie et. al., *High performance Pirani vacuum gauge*, Journal of Vacuum Science & Technology (1995), **13**

[71] K. Jousten, *Ultrahigh vacuum gauges*, Physikalisch-Technische Bundesanstalt (2007), pg. 150-151

[72] *Turbo Molecular Pump STP-A2203 series Specification*, https://www.lesker.com

[73] *HiPace® 700, for TCP 350, DN 160 CF-F*, https://www.pfeiffer-vacuum.com

[74] *Molflow+*, https://molflow.web.cern.ch/

[75] M. Ady, *Molflow 2.6 algorithm*, CERN (2016).

[76] R. Grinham, A. Chew, *A Review of Outgassing and Methods for its Reduction*, Appl. Sci. Converg. Technol. (2017) **26(5)**, pg. 99

[77] G. Borionetti, et. al., *Metal and organic contamination effects on the characteristics of thin oxides thermally grown on silicon based wafers*, Nuc. Inst. and Meth. in Phys. Res. B 253 (2006) pg. 278-281

[78] S. Melanson, et. al., *The Production of Negative Carbon Ions with a Volume Cusp Ion Source*, Proceedings of IPAC2016 (2016), pg. 2620-2622

[79] R.C. Shiell, X.K. Hu, Q.C.J. Hu, J.W. Hepburn, *Electron affinity determinations*, *NIST Chemistry WebBook, SRD 69*, (2000).

[80] P.Reinhed, et. al., *Precision Lifetime Measurements of He^- in a Cryogenic Electrostatic Ion-Beam Trap*

[81] R. McWeeny, *The electron affinity of H_2: a valence bond study**, Journal of Molecular Structure (Theochem), (1992), pg 403-413.

[82] H. Kreckel, et. al., *Metastable states of diatomic hydrogen anions*, XXVIII ICPEAC 2013, Journal of Physics, **488** (2014).

[83] R. Golser, et. al., *Experimental and Theoretical Evidence for Long-Lived Molecular Hydrogen Anions H_2^- and D_2^-*, Phys. Rev. Lett. **94** (2005).

[84] Y.K. Bae, et. al., *Observation of the metastable negative argon ion Ar^-*, Phys. Rev. Lett. **54**, (1985), pg. 789.

[85] K.M. Ervin, et. al., *The Only Stable State of O_2^- Is the $X\ ^2\Pi_g$ Ground State and It (Still!) Has an Adiabatic Electron Detachment Energy of 0.45eV*, Journal of Phys. and Chem. A, **107** (2003), pg. 8521-8529.

[86] G. Delaygue, *Oxygen Isotopes*, Encyclopedia of Earth Sciences Series (2009) pg. 666-673.

[87] S.R. Alger, J.A. Rees. *Positive and negative ion reaction in carbon dioxide*, J. Phys. D: Appl. Phys. **10** (1977) pg. 957-968.

[88] S. Melanson et. al., *The Extraction of Negative Carbon Ions from a Volume Cusp Ion Source*, AIP Conference Proceedings (2017).

[89] S.H. Lee, et. al., *"Associative" Electron Attachment to Azabenzene-$(CO2)_n$ van der Waals Complexes: Stepwise Formation of Covalent Bonds with Additive Electron Affinities*, J. Am. Chem. Soc. **139** (2008).

[90] G.L. Gutsev, R.J. Bartlett, R.N. Compton, *Electron affinities of CO_2, OCS, and CS_2*, J. Chem. Phys. **108** (1998) pg. 6756-6762.

[91] N.M. Jordan et. al., *Electron Emission near a Triple Point*, IEEE International Power Modulators and High-Voltage Conference (2008), pg. 311.